universität wien

MASTERARBEIT / MASTER'S THESIS

Titel der Masterarbeit / Title of the Master's Thesis

„Internal rotation profiles of red giants in the Kepler field"

verfasst von / submitted by

Stefanie Schauer BSc

angestrebter akademischer Grad / in partial fulfilment of the requirements for the degree of

Master of Science (MSc)

Wien, 2023 / Vienna, 2023

Studienkennzahl lt. Studienblatt / degree programme code as it appears on the student record sheet:	UA 066 861
Studienrichtung lt. Studienblatt / degree programme as it appears on the student record sheet:	Masterstudium Astronomie
Betreut von / Supervisor:	Dr. Thomas Kallinger

Acknowledgements

Foremost, I would like to express my deepest appreciation to my supervisor Dr. Thomas Kallinger whose passion for Asteroseismology inspired me. Whenever I had any concerns during the elaboration of this master's thesis, he showed profound belief in my work and abilities. Thank you for all the fruitful discussions, advice, and unwavering support you gave me. I would also like to extend my deepest gratitude to my dear friend and colleague Kathi, who had become a true friend over the last decade and never let me down. Thank you for all the laughter, scientific discourse, and motivation we shared. Let's keep pushing the limits.

Special thanks to my boyfriend Markus for his unconditional support, whether it was during a mental breakdown, or while fooling around when I successfully solved a scientific problem - you always make me laugh. Never lose that special ability.

My heartfelt thanks also go to my family for their financial and emotional support. Thank you for loving me the way I am and giving me the freedom to chase my dreams. I especially thank my dad for teaching me how to debug and be patient while programming, and my mom for always letting me shine bright. Further, I very much appreciate the countless hours playing Super Mario with my little sister. The less time I had, the more I needed it to let my thoughts rest.

Abstract

Internal rotation and the corresponding angular momentum transport are still poorly understood and raise many questions. Although stellar evolution models show an astonishing accuracy, they fail to reproduce the core rotation rate by simply assuming angular momentum conservation. The occurrence of mixed modes, i.e., a coupling between gravity modes in the radiative core and pressure modes in the convective envelope, in evolved stars allow, probing the physical core condition. It is crucial to examine the evolution of the core for various masses at distinct evolutionary state of the star to be able to set constraints on the angular momentum distribution inside stars.
The NASA[1] satellite *Kepler* has recorded long, uninterrupted, and high-accuracy photometric time series, allowing to probe the internal rotation of stars. The mean core rotation rates of over 6000 Kepler stars with various mass ranges along their evolution from the sub-giant up to the asymptotic giant branch are obtained by an automated measurement of the rotational splitting of dipole mixed modes, which empirically follow a Lorentzian distribution. This method is independent of the determination of $\Delta\Pi_1$, has estimated the location of the pure pressure mode, and also works beyond the confusion limit.
Rotation profiles have been successfully extracted for a total of 1286 stars, which is currently the largest data set available. Stars settle at the bottom of the red giant branch, where then the core rotation presents a steep but continuous slow down along their evolution to the tip of the red giant branch. For red clump stars, i.e. stars burning helium in their core, the core rotation rates are spatially limited between 10 and 12 $R_\odot$ and show only a shift towards higher radius compared to the rotation rates obtained at the tip of the red giant branch.
The interpretation of measured rotational splittings lead to the conclusion that the stellar core significantly slows down on the red giant branch. This works extends the available data pool of core rotation rates and underlines previous findings that there is a clear decline in the core rotation rate rather than a constant core evolution.

[1]National Aeronautics and Space Administration

Kurzfassung

Die Rotation im Sterninneren und der damit verbundene Drehimpulstransport werden noch nicht vollständig verstanden und es treten weiterhin viele Fragen auf. Obwohl Sternentwicklungsmodelle eine erstaunliche Genauigkeit aufweisen, können diese die Kernrotationsrate, unter der alleinigen Annahme von Drehimpulserhaltung, nicht reproduzieren. In Sternen, die bereits die Hauptreihe verlassen haben, treten gemischte Schwingungsmoden auf, die eine Kopplung zwischen Gravitationsmoden im radiativen Kern und Druckmoden in der konvektiven Hülle aufweisen. Sie ermöglichen die Untersuchung des physikalischen Kernzustandes. Um die Drehimpulsverteilung im Inneren von Sternen möglichst genau untersuchen zu können, ist es entscheidend, die Entwicklung des Kerns von Sternen mit verschiedenen Massen in unterschiedlichen Entwicklungsstadien zu untersuchen.
Der NASA[1]-Satellit *Kepler* hat lange, ununterbrochene und hoch präzise photometrische Zeitreihen aufgezeichnet, die es ermöglichen, die Rotation im Inneren der Sterne zu untersuchen. Die Kernrotationsraten von über 6000 Kepler-Sternen in verschiedenen Massenbereichen und Entwicklungszuständen entlang des Riesenastes werden durch eine automatisierte Messung der Rotationsaufspaltung von gemischten dipolaren Moden ermittelt. Sie folgen empirisch einer Lorentz-Verteilung. Diese Methode ist unabhängig von der Bestimmung des Periodenabstandes von dipolaren Moden $\Delta\Pi_1$, schätzt den Ort der reinen Druckmoden ab und funktioniert auch jenseits der Verwirrungsgrenze.
Die Rotationsprofile wurden erfolgreich für eine Gesamtanzahl von 1286 Sternen extrahiert und stellen somit den derzeit größten verfügbaren Datensatz dar. Am unteren Ende des Roten Riesenastes zeigt die stellare Kernrotation ein steiles, aber kontinuierliches Bremsen entlang ihrer Entwicklung zur Spitze des Roten Riesenastes. Bei sogenannten "red clump"-Sternen, die Helium in ihrem Kern verbrennen, sind die Kernrotationsraten zwischen 10 und 12 $R_\odot$ räumlich begrenzt und zeigen nur eine Verschiebung zu höheren Radien im Vergleich zu den Rotationsraten an der Spitze des Roten Riesenasts.
Die Interpretation der gemessenen Rotationsaufspaltungen führte zu dem Schluss, dass der Sternkern auf dem Roten Riesenast deutlich langsamer wird. Diese Arbeit erweitert den aktuell verfügbaren Datensatz und unterstreicht frühere Erkenntnisse, dass es eher ein deutliches Abbremsen, als eine konstante Kernrotationsrate entlang der Roten Riesenentwicklung ist.

[1]National Aeronautics and Space Administration

Contents

Acknowledgements i

Abstract iii

Kurzfassung v

List of Tables ix

List of Figures xi

1. Introduction 1

2. A brief history of asteroseismology 3
- 2.1. Stellar oscillations across the HR diagram 3
- 2.2. Stellar pulsations 5
  - 2.2.1. Mode properties 6
  - 2.2.2. Asymptotic theory of stellar oscillations 8
- 2.3. Excitation mechanisms 11
- 2.4. Solar-like oscillators 13
  - 2.4.1. (Non-) linear seismic scaling relations 16

3. Stellar evolution in a coco-nutshell 19
- 3.1. The seismic HR diagram: $\Delta\Pi_1$ - $\Delta\nu$ 19
  - 3.1.1. Main-sequence and Schönberg-Chandrasekhar limit 19
  - 3.1.2. Giant evolution 20

4. Stellar Rotation 25
- 4.1. During subgiant evolution 25
- 4.2. Along the red giant branch 26
- 4.3. In the clump 28

5. Data 31
- 5.1. An observational history 31
  - 5.1.1. The NASA Kepler and K2 mission 31
- 5.2. Data 32

6. Method 35
- 6.1. Choosing targets 35

6.2. Modulation of the rotational splittings 36
6.3. Scanning the dipole mode spectrum 38
6.4. Identifying the real rotational splitting 41
6.5. Estimating the mean core rotation period $\langle T_{\mathrm{rot}} \rangle_c$ 44

7. Results and Discussion **45**
7.1. Comparison with other measurements 47
7.2. Evolution of the core rotation 49
7.3. Slow-down along the red giant branch 53

8. Conclusion **57**

Bibliography **59**

A. Appendix **65**

List of Tables

2.1. Periods and amplitudes for various pulsating groups 5

4.1. Mean core rotation rates for stars obtained by other authors 27

5.1. Count of stars, and modes with spherical degree from l = 0 to 3 34
5.2. Output parameter of ABBA 34

6.1. Reduced data sample 36

7.1. Final sample including at least 3 multiplets 45
7.2. Measured slow-down rates as a function of stellar radius for stars on the red giant branch 54
7.3. Measured slow-down rates and mean rotational splittings for different mass ranges 55

List of Figures

2.1. Schematic illustration of pulsating stars in a Hertzsprung-Russel diagram 4
2.2. Spherical harmonics for radial and non-radial modes 7
2.3. p and g modes as a function of frequency and spherical degree 9
2.4. Propagation diagram 11
2.5. Mode inertia and amplitude versus frequency 12
2.6. The solar amplitude spectrum 13
2.7. Échelle diagram of the solar-type star KIC 11395018 15

3.1. Asteroseismic Hertzsprung-Russell diagram 23

4.1. Evolution of the core rotation of subgiants, red giants, and clump stars . . 28

5.1. Detection of solar-like oscillations pre-2009, by CoRoT, and Kepler 32
5.2. Seismic Hertzsprung-Russel diagram for the APOKASC sample 33

6.1. Flow chart of the code 37
6.2. Histogram of KIC 8605197 and KIC 1438803 39
6.3. Échelle diagrams of KIC 7533995, KIC 8605197, and KIC 1433803 40
6.4. Region of the potential split-component 41
6.5. Rotational splittings fitted with a Lorentzian function for KIC 1433803 and KIC 8605197 42

7.1. Completeness analysis of the results 46
7.2. Identification of overlapping split components 46
7.3. Rotational splittings, λ, and β 47
7.4. Comparison of rotational splitting with measurements from others 48
7.5. Evolution of the mean core rotation period for stars on the red giant branch 49
7.6. Mean core rotation rate along stellar evolution 51
7.7. Mean core rotation rate along stellar evolution with a fit 52
7.8. Measured slow-down rates for stars on the red giant branch 53
7.9. Slow-down rates separated according to specific mass ranges 54

1. Introduction

One of the most astonishing phrases I came across during the development of this master's thesis on what *Asteroseimology* is, is as simple and beautiful as it sounds:

"Seeing with sound"

Although it is not possible to actually *"look"* inside a star, its intrinsic brightness variations, which change periodically due to oscillations, provide a unique opportunity to probe the hidden world inside a star. The modes observed at the surface propagated through different stellar regions, can be damped and/or (re-)excited, but most importantly contain valuable information. Basically, there are two main types of modes: pressure *"p"* or acoustic modes, which are mostly sensitive to the convective envelope with pressure being their restoring force, and gravity *"g"* modes, which are mostly sensitive to the radiative interior with buoyancy being the corresponding restoring force. Depending on stellar evolution, modes show different behavior. In solar-like main-sequence stars, only p modes are found. This behavior changes when the star evolves towards the bottom of the red giant branch. During this transition, p and g modes start to couple being both, sensitive to the core regions and to the stellar envelope. The so-called *mixed modes*, or especially the dipole mixed modes, are particularly sensitive to the red giant core and give access to the desired near-core rotation rates.
Rotation has an unprecedented impact on the stellar structure and evolution and is still one of the main uncertainties in stellar modelling. The evolution of rotation in the stellar interior is still poorly understood and challenges modern stellar astrophysics. The observed differential rotation in stars behaves differently than predicted by stellar evolution models. Generally, it is expected that the core spins up on the red giant branch, because at this stage of stellar evolution the core contracts while the envelope expands. Astonishingly, seismic measurements revealed that the core rotation rates are much lower than predicted by stellar evolution models considering hydrodynamical processes only. This mismatch between observations and model predictions concludes that there must be a yet unknown mechanism at work that redistributes angular momentum inside a star.

The aim of this master's thesis is to extend the available data of mean core rotation rates to find new constraints concerning the redistribution of angular momentum throughout the various evolutionary phases, and beyond that, the improvement of stellar evolution models.
A first brief dive into the exciting world of asteroseismology will be given in Chapter 2. Hereafter, in Chapter 3 stellar evolution of evolved stars is discussed with focus on the low- and intermediate-mass stars up to roughly 2.2 $M_{\odot}$ as this covers the mass range investigated within this master's thesis. The evolution of stellar core and envelope rotation

for subgiants, red giants and secondary clump stars are outlined in Chapter 4 to give an overview on the current scientific situation. The *NASA* satellite *Kepler* has recorded long, uninterrupted, and high-photometric times series, which enable an investigation on the internal rotation of stars with various masses along with their evolution from the main-sequence up to the core-helium burning phase. The corresponding data set consisting of more than 6000 Kepler stars is introduced in Chapter 5. The extracted modes including the radial mode with spherical degree $l = 0$ and the non-radial dipole modes mixed modes $(l = 1)$ are used to identify the corresponding rotational splitting, and thereafter, the mean core rotation rate. The whole process is outlined in great details in Chapter 6. Finally, the results and their interpretation are presented in Chapter 7, where I investigated its validity by comparing the results with other scientific measurements, present the evolution of the core rotation and probe a potential mass dependence correlated with the core rotation rate.

2. A brief history of asteroseismology

Stars are gaseous spheres that can oscillate in many different modes if suitably excited. Measuring and interpreting these oscillations is the key to the hidden worlds inside a star. The frequencies of these modes depend on distinct properties of the region through which the wave travels, e.g., density, temperature, and gas motions. The corresponding amplitudes are constraint by excitation and damping mechanisms, which may get disturbed by convection, opacity variations, and magnetic fields. This frequency spectrum puts strong constraints on the internal stellar structure and yields information about composition (and age), mixing, and internal rotation that cannot be obtained in any other way. Thus, it is of great interest to study the frequencies and amplitudes of various stars of different types to improve our understanding of stellar structure and evolution.

2.1. Stellar oscillations across the HR diagram

A star whose brightness varies periodically, semi-periodically, or irregularly is called a *variable star*. In this case, the brightness changes are caused by physical phenomena and not by evolutionary effects. Furthermore, variable stars are categorized according to the origin of their variability, e.g., *extrinsic* and *intrinsic* variables. Extrinsic variables are objects, whose light curve variability is caused by geometrical effects, like eclipsing binaries, or effects of stellar rotation. Rotating stars can exhibit brightness changes due to spots on the stellar surface. Whereas in the latter group, variation is caused by physical changes occurring in the star itself (Eyer and Mowlavi, 2008).
Stellar oscillations are found in nearly all phases of stellar evolution, as illustrated in Fig. 2.1. To get a first impression on the variability, some examples of different classes of pulsating stars, including their light curve properties, are shown in Tab. 2.1. Nevertheless, there exists a rather dense region including several stellar classes, which is marked by two parallel dashed lines, and is called the *classical instability strip*. It roughly demonstrates the border at which the two main driving mechanisms can be separated for low- and intermediate-mass stars. On the hotter left side, pulsation is driven by an opacity mechanism (see more details in Sec. 2.3), which is populated by Cepheids, RR Lyrae, δSct stars, and rapidly oscillating Ap (roAp) stars.
In stars with an outer convective envelope located to the cooler right side of the instability strip, oscillations are intrinsically damped but stochastically excited due to the near surface convection (Houdek et al., 1999). This includes stars on the main-sequence up to about 1.5 $M_{\odot}$, and the subsequent evolution from the giant to the asymptotic giant branch. Mira variables and semi-regular variables are indeed located on the red side of

the instability strip, although their oscillation is heat-driven. They consist of a partial ionization zone combined with an effective convection, and are thus said to be heat-driven (Aerts et al., 2010).

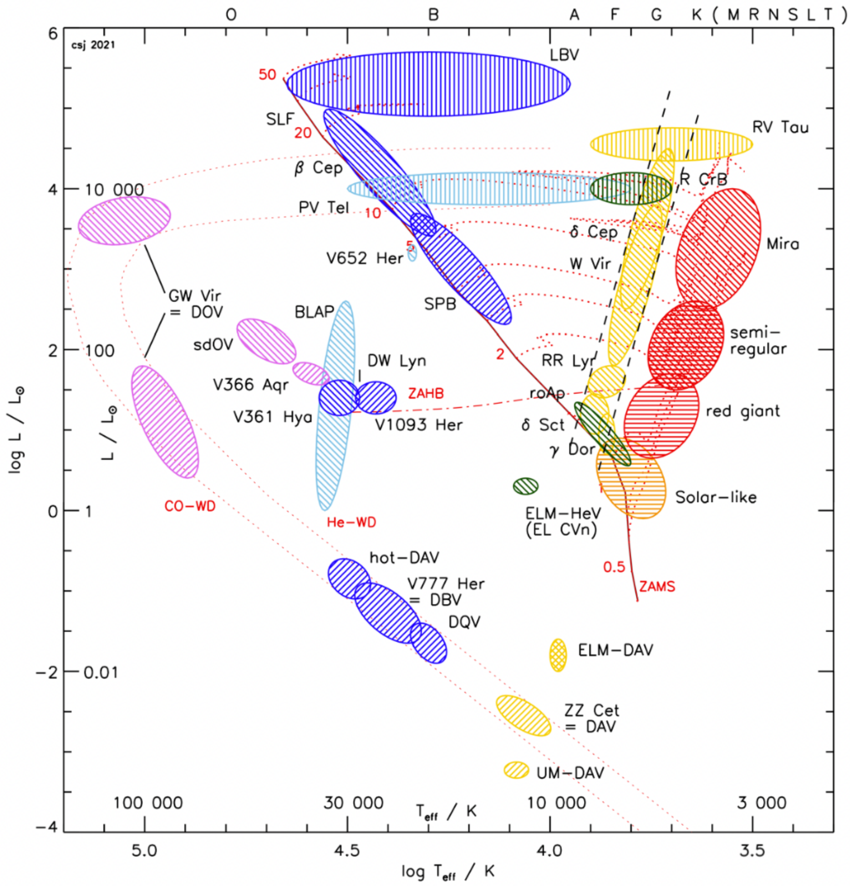

Figure 2.1.: Schematic illustration of distinct groups of pulsating stars. The red solid line depicts the zero-age-main-sequence, the red numbers show typical masses in $M_\odot$ along the main-sequence in addition to their different evolutionary paths marked as dotted line. The black dashed lines show the position of the theoretical instability strip. The various hatched regions represent the primary type of oscillating mode: p modes (\\\\\\), g modes (///), stochastically driven pulsators (≡), and strange modes (|||). Figure taken from Kurtz (2022).

Position in HRD	Class	Period	Amplitude [mag]
main-sequence OBAF stars	γ Dor	8 h - 3 d	up to few 0.1
	δ Scuti	30 min - 6 h	up to few 0.1
	roAp	5 - 20 min	up to 0.01
	SPB	0.5 - 5 d	up to 0.03
	β Cephei	2-12 h	up to 0.05
hot side of the instability strip	RR Lyrae	5h - 1.1 d	0.2-2
	W Vir	1 - 20 d	0.3 - 1.2
	Cepheids	2 - 70 d	0.1 - 1.5
	RV Tau	30 - 150 d	1 - 3
cool side of the instability strip	solar-like stars	few min	$\sim$ 10 ppm
	solar-like giants	few h - days	0.1 - 10 mmag
	Semiregular variables	30 - 1000 d	1 - 2
	Mira	50 - 1000 d	up to 8
white dwarf stars	GW Vir	5 min - 80 min	up to 0.2
	V777 Her	1 - 20 d	up to 0.2
	ZZ Ceti	0.5 - 25 min	up to 0.2

Table 2.1.: Examples of some pulsating variable stars, including their distinct periods and amplitudes. Periods are displayed in seconds (s), minutes (min), hours (h), or days (d), whereas the amplitudes are in magnitudes (mag). Data taken from Eyer and Mowlavi (2008).

2.2. Stellar pulsations

Asteroseismology allows to investigate the internal structure of pulsating stars according to their oscillation frequencies observable at the stellar surface. The frequency of a pulsation mode is affected by the properties of the region it runs through. It thus provides the desired information about the internal structure of the star, e.g., the density distribution. Although the characterisation of these properties is not trivial, several approximations can be used, but at first the characteristics of pulsation modes have to be discussed.

Relevant timescales

If a star deviates from hydrostatic equilibrium, evolution occurs on its own characteristic timescale. The following timescales are calibrated to the Sun in order to get an estiamted duration of each timescale. The shortest timescale is the *dynamical timescale*, which expresses the time a star needs to restore its hydrostatic equilibrium from a disturbance.

$$\tau_{\rm dyn} \simeq \sqrt{\frac{R_\odot^3}{GM_\odot}} \simeq \sqrt{\frac{1}{G\bar{\rho}_\odot}} \simeq 30\text{min} \tag{2.1}$$

With the gravitational constant $G = 6.67 \times 10^{-11} m^3/kg/s^2$, $R_\odot = 6.96 \times 10^8 m$, and $M_\odot = 1.99 \times 10^{30} kg$ being solar radius and mass, respectively. The *Kelvin-Helmholtz* *timescale* defines the time it takes a star to contract without any nuclear energy source, while all energy is radiated at the surface:

$$\tau_{\mathrm{KH}} \simeq \frac{GM_{\odot}^2}{R_{\odot}L_{\odot}} \simeq 3 \times 10^7 \mathrm{yr} \tag{2.2}$$

where $L_{\odot} = 3.86 \times 10^{26} W$ is the solar luminosity. Finally, the *nuclear timescale* defines the time required until the nuclear energy reservoir is exhausted at a given luminosity:

$$\tau_{\mathrm{nuc}} \equiv \frac{0.007 M_{\odot} c^2}{L_{\odot}} \approx 10^{11} \mathrm{yr} \tag{2.3}$$

with a mass deficit of 0.7 % for hydrogen fusion. To conclude: $\tau_{\mathrm{dyn}} \ll \tau_{\mathrm{KH}} \ll \tau_{\mathrm{nuc}}$ (e.g. Maeder (2009)).

2.2.1. Mode properties

Low-amplitude oscillations can be treated as small perturbations to the equilibrium structure. In general, they are described by a linearized perturbation analysis of the general equations of hydrodynamics, i.e., the conservation of mass, momentum, and energy. The solutions of the equation of motion for a spherical symmetric star has displacements ξ in the directions (r, θ, ϕ), where r is the distance to the centre, θ is the co-latitude, measured from the pulsation pole, and ϕ is the longitude. Thus, e.g., the radial component of the displacement ξ_r is the real part of:

$$\xi_r(r, \theta, \phi, t) = a(r) Y_l^m(\theta, \phi) e^{-i\omega t} \tag{2.4}$$

where $a(r)$ is the amplitude, ω is the angular frequency (or cyclic frequency for $\nu = \omega/2\pi$) and $Y_l^m(\theta, \phi)$ are spherical harmonics given by:

$$Y_l^m(\theta, \phi) = (-1)^m \underbrace{\sqrt{\frac{2l+1}{4\pi} \frac{(l-m)!}{(l+m)!}}}_{\substack{c_{lm}=\text{normalization} \\ \text{constant}}} P_l^m(\cos\theta) e^{(im\phi)} \tag{2.5}$$

The *Legendre polynomials* $P_l^m(\cos(\theta))$ for degree l > 0 and azimuthal order m range from $-l$ to $+l$, thus there are $2l + 1$ modes for each degree l:

$$P_l^m(\cos\theta) = \frac{1}{2^l l!} (1 - \cos^2\theta)^{m/2} \frac{d^{l+m}}{d\cos^{l+m}\theta} (\cos^2\theta - 1)^l \tag{2.6}$$

Each oscillation mode of a star is characterized by three discrete spherical harmonic quantum numbers:

- n = *radial order*; number of radial nodes
- l = *degree*; count the number of present surface nodes
- m = *azimuthal order*; number of nodal lines crossing the stellar equator

The values of m range from -l to $+l$ propagating retrograde and prograde, respectively. Hence, there are $2l+1$ modes for each degree l. The simplest oscillation modes are the *radial* modes with a spherical degree equal to zero. Amongst these modes, is the *fundamental* mode with no radial nodes, where the star expands and contracts, while keeping its spherical symmetry. The number of *overtones* of a radial mode gives the number of nodes within a star along concentric shells (Aerts et al., 2010).
In a more general way, oscillation modes can be described by *non-radial* pulsation, where the simplest one is the so-called *dipole* mode, with l equals one, m equals zero, and the equator being a node. Furthermore, non-radial modes must include at least one radial node, thus $n \geq 1$. The stellar surface is divided into regions depending on the count of spherical degree. Due to partial cancellation, the detection of modes becomes more difficult as their degree increases. A schematic visualization of distinct stellar surfaces is illustrated in Fig. 2.2 (Aerts et al., 2010).

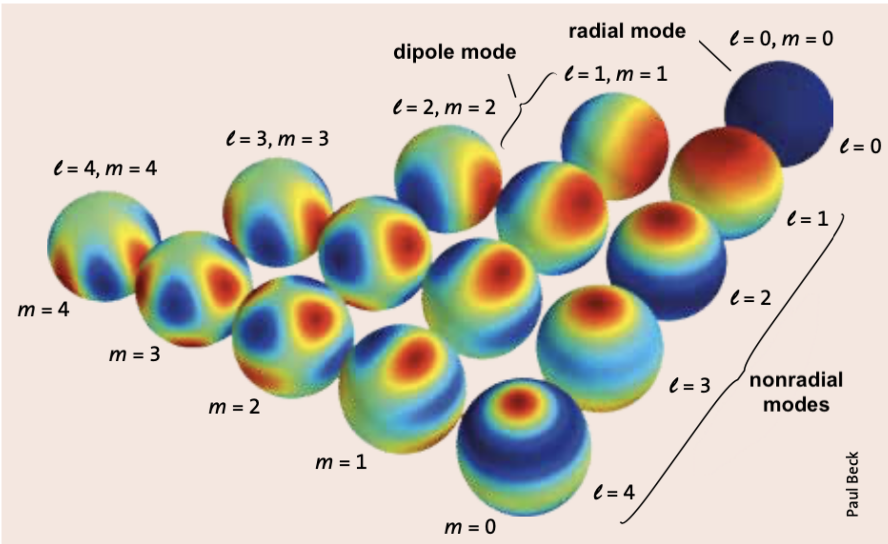

Figure 2.2.: Examples of spherical harmonics with different spherical degrees l and azimuthal order m. The green bands show the position of the surface nodes, whereas the colour-coding represents sections in motion either moving inwards (heating) or outwards (cooling) at any given time, then vice versa. Figure taken from Beck and Kallinger (2013).

Stellar pulsation is described by distinct types of pulsation modes according to their nature and restoring force when a star is forced of its equilibrium status. There exist five restoring forces: pressure (p modes), buoyancy (gravity or g modes), Coriolis force (inertial and Rossby, r modes), magnetic (Alfvén), and tidal forces, which can also operate together. As an example, the Coriolis force combined with gravity results in the so-called *gravito-inertial modes*, or the magnetic Lorentz force along with pressure give rise to the so-called *magneto-acoustic modes* (Kurtz, 2022). Although these are beyond the scope of this work. As the main restoring forces are pressure and gravity, this master's thesis will solely focus on them.
In Fig. 2.3 the mode frequencies versus their spherical degree l based on a solar model is shown. The typical behaviour of the two distinct modes is discussed in more detail below. Note here that the continuous mode lines are just for illustration, usually they are discrete points.

- p modes: acoustic or pressure modes are predominately driven by pressure fluctuations, and are specially sensitive to the conditions of the outer stellar envelope. Pressure modes have higher frequencies, which increase with increasing radial overtone n and spherical degree l. Given the asymptotic approximation (see Sect. 2.4), high overtone p modes (n $\gg$ l) frequencies are roughly equally spaced in frequency, with spacings depending on the large separation $\Delta\nu$ (Kurtz, 2022).

- g modes: density or gravity modes are primarily sensitive to the deep stellar interior. Gravity modes have lower frequencies, which decrease with higher overtone n, but increase with spherical degree l. High overtone g mode (n $\gg$ l) frequencies are equally spaced in period with spacings asymptotically approaching the characteristic period spacing Π_0, giving the buoyancy travel time across the star (Kurtz, 2022).

Although each of the mode types are separated in their cavities with no interaction in main-sequence stars, there is the phenomenon for evolved stars that couples g and p modes, giving raise to the so-called *mixed modes*. Mixed modes can be observed due to the large density gradient outside the helium core, and thus contain information about the core regions in addition to the envelope (Aerts et al., 2010).

2.2.2. Asymptotic theory of stellar oscillations

The properties of adiabatic non-radial oscillations provide a powerful tool to evaluate the diagnostic potential of solar-like oscillations in giant stars. It is convenient to simplify the complex system of differential equations by using approaches like assuming oscillations have to be adiabatic, which excludes effects of damping and excitation. This simplification is legit because pulsation takes place on τ_{dyn} (Eq. 2.1), which is short compared to the τ_{KH} (Eq. 2.2). Thus, the deviations from adiabacity are negligible in most stellar regions. In general, solar-like oscillations are of high radial order, such that eigenfunctions vary much more rapidly than the equilibrium quantities. The analysis of this behaviour, correlated with stellar structure, provides the desired information. Another simplification, which can be performed due to the "high radial" or "high degree" order of stars, is

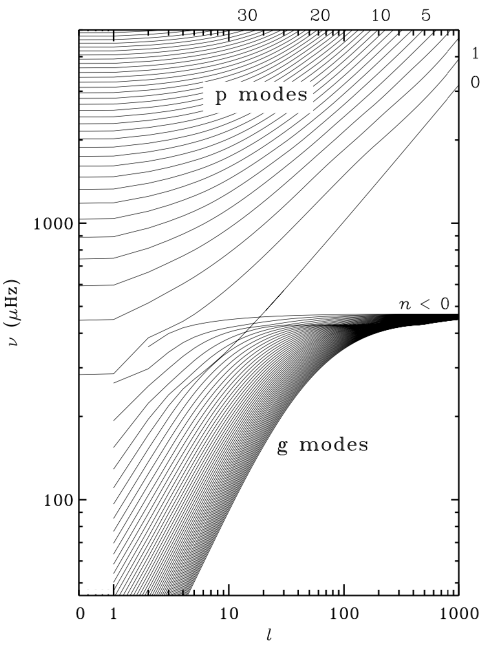

Figure 2.3.: The frequency versus their spherical degree l of modes for a solar model. It illustrates that p modes increases with overtone n and degree l. The values of overtone n are given in the top right side of the figure. Gravity modes have lower frequencies than p modes, which decrease with n but increase with degree l. Figure taken from Aerts et al. (2010).

the so-called *Cowling approximation* (Cowling, 1941). It reduces the four equations of adiabatic oscillations to a second-order system, while neglecting the perturbation to the gravitational potential. Finally, the equations are often expressed as:

$$\frac{d^2\xi_r}{dr^2} = \frac{\omega^2}{c_s^2}\left(1 - \frac{N^2}{\omega^2}\right)\left(\frac{S_l^2}{\omega^2} - 1\right)\xi_r = -K_s(r)\xi_r \tag{2.7}$$

where ξ_r is the radial displacement, ω is the angular frequency, c_s the adiabatic sound speed with $c_s^2 = \Gamma_1 p/\rho$, where p is the pressure, ρ is the density and $\Gamma_1 = (\partial \ln p/\partial \ln \rho)_{ad}$ gives the adiabatic exponent, N the buoyancy frequency (or *Brunt-Väisälä frequency*) and S_l is the acoustic frequency (or *Lamb frequency*). It is deduced from Eq. 2.7 that the characteristic frequencies S_l and N determine the oscillatory behaviour:

- **Lamb** frequency S_l:

$$S_l^2 = \frac{l(l+1)c_s^2}{r^2} \tag{2.8}$$

with r being the radius. The Lamb frequency is the local characteristic frequency of horizontal propagating sound waves with wavenumber $k_h = \sqrt{l(l+1)}/r$.

- **Brunt-Väisälä** frequency N:

$$N^2 \simeq \frac{g^2\rho}{p}(\nabla_{ad} - \nabla + \nabla_\mu) \tag{2.9}$$

with g being the local gravitational acceleration, derived with the equation of state for a fully ionized ideal gas: $\nabla_{ad} = (\partial \ln T/\partial \ln p)_{ad}$, $\nabla = (d\ln T/d\ln P)$, and $\nabla_\mu = d\ln\mu/d\ln p$, where T is the temperature and μ is the mean molecular weight.

Both characteristic frequencies provide the key to determine the behaviour of oscillations, as can be seen in Fig. 2.4 for a solar model. The buoyancy frequency (solid line) and the acoustic frequency (dashed lines) are illustrated along the fractional radius r/R with the corresponding cyclic frequency ν $(= \omega/2\pi)$. Obviously, the definition of the characteristic frequency N^2 depends on the convective instabilities and is thus negative in convection zones ($\nabla > \nabla_{ad} + \nabla_\mu$) and positive in convectively stable regions. Due to nuclear burning in the centre of the star, the mean molecular weight μ increases with increasing depth, and so does the pressure. Hence, providing a positive impact on the contribution to N^2. Pressure and gravity modes are trapped inside the so-called *mode cavities*. The boundaries of the mode cavities are known as *turning points*, where $K_s(r) = 0$ (Eq. 2.7). For $K_s(r) > 0$ the solution oscillates. Gravity modes with low frequencies are trapped whenever their frequency is below the Brunt-Väisälä frequency and the Lamb frequency ($|\omega| > |N|$ and $|\omega| > |S_l|$), while p modes with high frequencies are trapped whenever their frequency is above the Lamb frequency ($|\omega| < |N|$ and $|\omega| < |S_l|$). Under these conditions, modes correspond to standing waves in their cavity. Finally, the solution for ξ_r is exponential if $|N| < |\omega| < S_l$ or $S_l < |\omega| < |N|$, and refers to the so-called *evanescent regions*, where the eigensolutions decrease or increase exponentially the farther away they are from the mode cavity (Aerts, 2021).

Stellar evolution is accompanied by structural changes inside the star, e.g., the increasing density gradient, which drastically influences the sound speed c_s(r), and hence S_l. As a result, the mode cavities decrease in frequency and the evanescent regions become narrower. Their exponential decay can thus reach the g mode cavity and couple to the eigenfrequencies of the g modes. This behaviour can be observed in dipole modes in red giants, which are called *mixed modes*. These have a g-mode character in the deep interior of the star and a p-mode character in the outer stellar envelope. Thus, they are essentially to enter the hidden world inside a star, where usually only p modes are observable. Depending on the contribution of p and g mode, they are referred to as p-dominated mixed modes (*p-m modes*) and g-dominated mixed modes (*g-m modes*), respectively (e.g. Aerts et al. (2010), Hekker and Christensen-Dalsgaard (2017)).

Mode trapping

If non-radial modes are trapped in the core, they have a significant amount of kinetic energy in the g-cavity and low kinetic energy in the p-cavity. Whereas modes trapped in

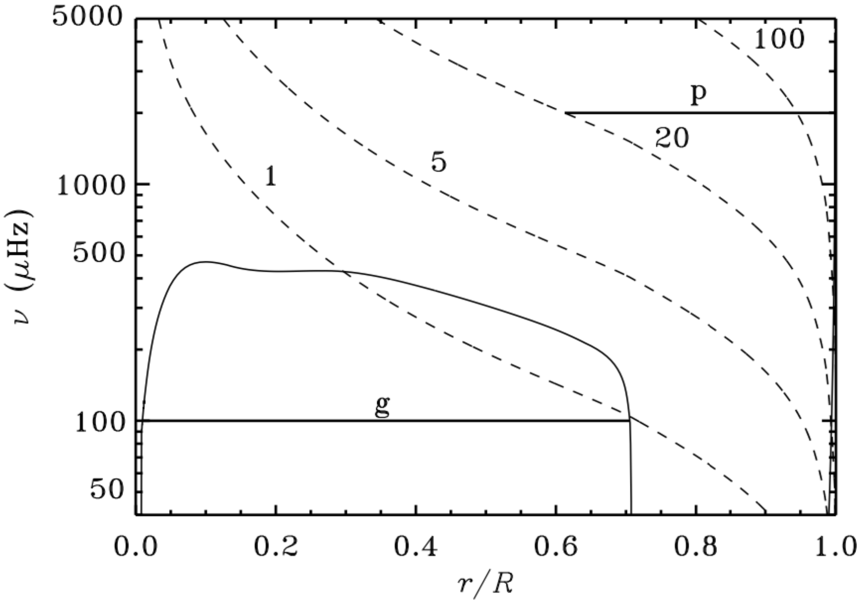

Figure 2.4.: Propagation diagram: illustration of the buoyancy frequency (solid line) and the acoustic frequency (dashed lines) for a distinct count of spherical degree l = 1, 5, 20 and 100 throughout a solar model. The two horizontal lines show the trapping regions for g modes (ν = 100 μHz) and p modes (ν = 2000 μHz), respectively. Figure taken from Aerts et al. (2010).

the envelope have high kinetic energy in the g-cavity and low one in the p-cavity. Mode trapping directly affects the mode inertia, as can be seen in Fig. 2.5 on the left for l = 0 to 2 modes. The high Brunt-Väisälä frequency causes a very dense spectrum. The l = 2 modes trapped in the envelope have a lower inertia than the l = 1 modes, while all other modes show contrary behaviour. The efficiency and size of the evanescent region increases with increasing degree. Non-radial dipole modes trapped in the core have very small amplitudes due to the large mode inertia and radiative damping (see right Fig. 2.5 for comparison). On the other hand, approximately between two consecutive radial modes, the non-radial modes show their highest amplitudes trapped in the envelope. Although the amplitudes are smaller than the ones for radial modes, both show similar inertia (Dupret et al., 2009). Fortunately, the trapping is not perfect, thus l = 1 mixed modes are observed throughout the spectrum, raising the opportunity to investigate the stellar interior (Mosser et al., 2012b).

2.3. Excitation mechanisms

Pulsation is a relatively stable phenomena, as can be seen in Sec. 2.1, and occurs in many stars. There are three major mechanisms that drive stellar pulsation.

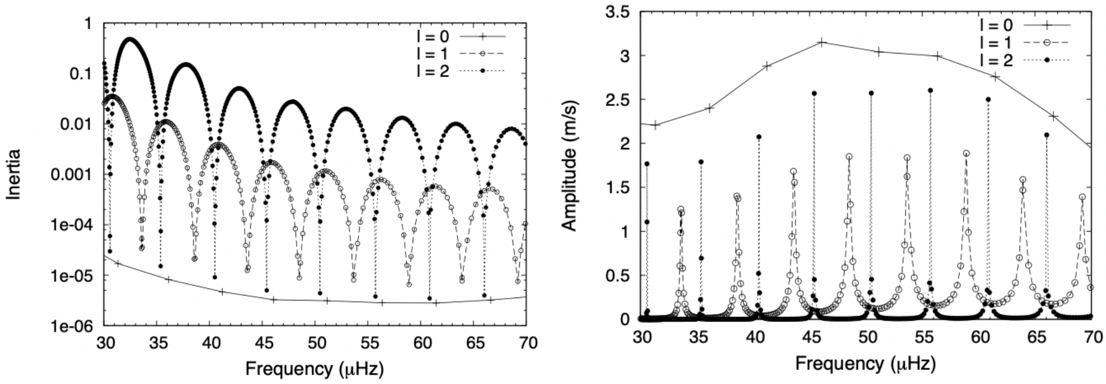

Figure 2.5.: Theoretical predictions for l = 0 to 2 modes of a $2M_{\odot}$ star on the red giant branch. *left*: mode inertia, *right*: amplitudes. Figure taken from Dupret et al. (2009).

During a pulsation cycle, energy is lost as the bulk of the star damps the pulsation. Excitation and damping needs to be outbalanced throughout the star to get a mode globally excited. A radial layer of a star that gains heat during compression drives the pulsation, whereas all other layers that lose heat during compression, damp the pulsation during a pulsation cycle. Thus, if the radial layer wins and drives the oscillation, the star converts thermal energy into mechanical energy like an *heat-engine*. In for example RR Lyrae, Cepheid variables, βCep and δScti stars, this process is connected with opacity, and thus named κ-mechanism (Aerts et al., 2010)
In the Sun, solar-like oscillators as well as in red giants, modes are intrinsically stable, and the κ-mechanism is out of order. These stars are said to be *stochastically* driven. The star oscillates in its natural oscillation frequencies, which are enhanced due to the acoustic energy in the outer convective region of the star. Thus, stochastic noise is transferred to energy of global oscillation.
Finally, there is the ϵ-*mechanism*, where variations of the energy generation rate, which is temperature dependent, in the stellar core could drive global pulsations. Although this is not yet found to be the only driving mechanism at work (Aerts et al., 2010).

κ-mechanism

Generally, an arbitrary perturbation in the partially ionized layer results in matter becoming compressed, which increases pressure, temperature, and hence opacity. The layer becomes optically thick, blocks the transfer of radiation outwards, and raises the radiation pressure below the layer. The strong radiation pressure lifts the layer, leading to a shift from equilibrium. To compensate this process, the layer expands, resulting in a decrease of pressure, temperature, and opacity. Due to the ionization of the gas, the layer becomes optically thin, and radiation pressure can escape. The layer moves back to its original position and a new pulsation cycle begins (Lamers and Levesque, 2017). The deeper oscillations penetrate into the star, the more adiabatic they become. Thus, this effect is small. The zones of ionization must encompass a sufficient amount of the stellar mass, so that excitation wins over damping. Therefore, they must be situated at a suitable depth. The surface temperature of a star decides about its stability via the κ mechanism. E.g., in main-sequence stars, the outer layers are too hot, resulting in fully ionized hydrogen and an almost complete ionization of helium. Therefore, the κ mechanism does not show much excitation (Kippenhahn et al. (2012), Maeder (2009)).

2.4. Solar-like oscillators

For obvious reasons, the Sun is the best-studied example of an oscillating star. Due to its proximity, it is possible to investigate oscillations with spherical degrees up to about l = 1500. Its numerous simultaneously oscillating modes provide an extraordinary set of data and information.

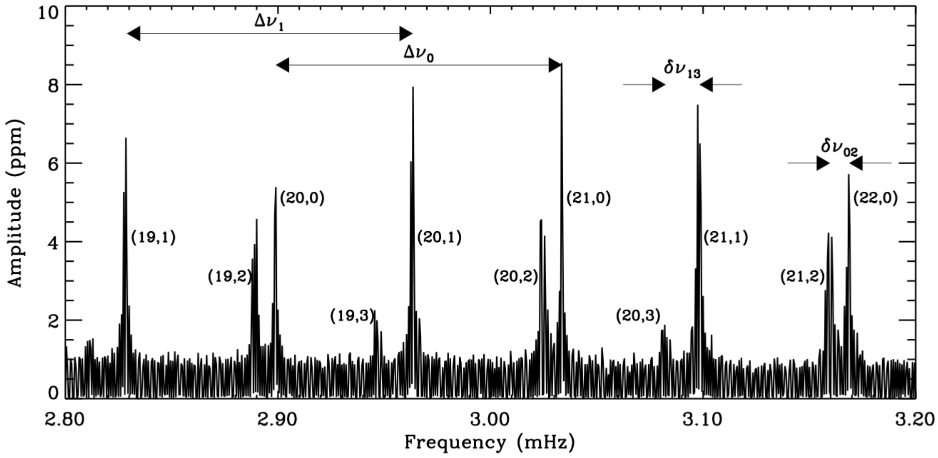

Figure 2.6.: The solar amplitude spectrum with their corresponding (n,l) values for each mode. The large frequency separation $\Delta\nu$ is a measurement for the mean stellar density, whereas the small frequency separation $\delta\nu$ provides information on the core composition, hence stellar age in case of main-sequence stars. Figure taken from Bedding and Kjeldsen (2003).

Asymptotic relation

The peaks in the amplitude spectrum of the Sun in Fig. 2.6 have evidently a highly regular frequency structure. Tassoul (1980) showed that frequencies of high-order and low-degree p modes oscillations follow an asymptotic relation:

$$\nu_{\rm nl} \simeq \Delta\nu\Big(n + \frac{l}{2} + \epsilon\Big) - l(l+1)\delta\nu_{\rm nl}/6 \tag{2.10}$$

where ϵ is the phase offset, $\Delta\nu$ and $\delta\nu_{nl}$ are the large and the small frequency separation, respectively. The *large frequency separation* is the difference between two consecutive modes of radial order and equal spherical degree. Further it can be described by the sound crossing time of an acoustic wave throughout the star, which is also an approximation for the stellar mean density (Ulrich, 1986):

$$\Delta\nu = \nu_{nl} - \nu_{n-1,l} = \left(2\int_0^R \frac{dr}{c_s}\right)^{-1} \propto \sqrt{\frac{M}{R^3}} \propto \sqrt{\bar{\rho}} \tag{2.11}$$

The *small frequency separation* is the difference in frequency between odd- and even-degree modes (e.g. Gough (1986)):

$$\delta\nu_{n,l+2} = \nu_{nl} - \nu_{n-1,l+2} \simeq \frac{\Delta\nu}{4\pi^2\nu_{nl}}\left(\int_0^R \frac{dc_s}{dr}\frac{dr}{r}\right) \tag{2.12}$$

The small frequency separation $\delta\nu_{nl}$ is sensitive to the core and its composition. It provides a measure for the helium abundance in the core, leading to an approximation of the stellar age, particularly if the investigated star is on the main-sequence (e.g. Ulrich (1986), Christensen-Dalsgaard (1984)).
Unfortunately, this effect cannot be obtained for subgiants and giants. Huber et al. (2010) noted that the relation of $\delta\nu_{02}$ scales with $\Delta\nu$. The cavity of p modes is constraint by the compact core and can therefore not measure the core composition and hence stellar age.

Phase term ϵ

The phase term ϵ is a dimensionless offset of radial modes in an échelle diagram, as in Fig. 2.7. In this diagram, the power spectrum is sliced into parts of $\Delta\nu$ and stacked bottom up. The resulting ridges show either the l = 0, 1 and 2 modes, respectively. When considering only the three central radial order around ν_{max}, where the central frequency ν_c and large separation Δ_ν are known:

$$\nu_{c,0} = \Delta\nu_c(n + \epsilon'_c) \tag{2.13}$$

The phase shift of the mode can be determined easily because $\epsilon'_c = (\nu_{c,0}/\Delta\nu_c)$ modulo 1. By plotting the phase shift of the central mode versus the central large frequency separation, one can distinguish between different evolutionary stages (Kallinger et al., 2012). In stars with an inert helium core, the second helium-ionization zone is at a different location than for stars with an active helium-burning core. This local difference causes small oscillatory deviations in the frequencies and therefore results in a distinct evolutionary phase (Hekker and Christensen-Dalsgaard, 2017).

Period Spacing $\Delta\Pi$

According to an asymptotic relation, gravity modes are evenly spaced in period space. Meaning that for any degree, the gravity mode appears with near constant period

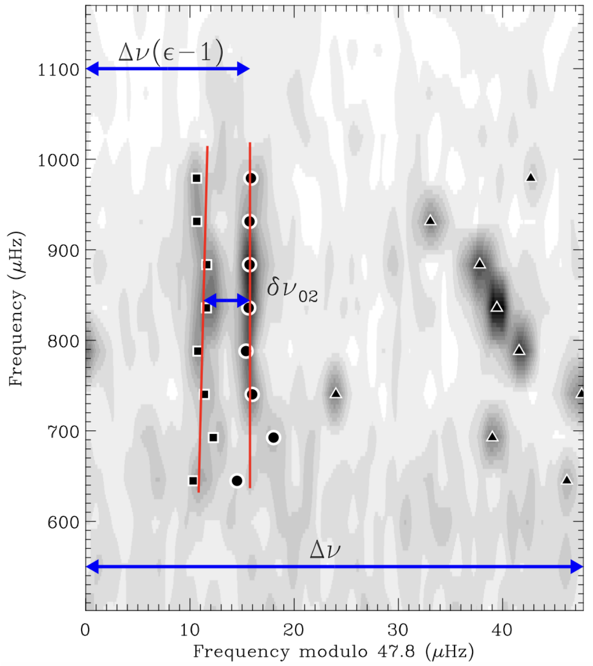

Figure 2.7.: Échelle diagram of a solar-type star KIC 11395018 showing mode frequencies for l = 0, 1, and 2 indicated as circles, triangles and squares, respectively. The values of the small separation between l = 0 and l = 2 ($\delta\nu_{02}$), the large separation $\Delta\nu$ (at $\nu_{\max}$) and the relationship $\Delta\nu(\epsilon-1)$ is illustrated in blue lines. Figure taken from White et al. (2011).

separation, the so-called *period spacing* $\Delta\Pi_l$:

$$\Delta\Pi_l = \Pi_0/\sqrt{l(l+1)} \tag{2.14}$$

with

$$\Pi_0 = 2\pi^2\Big(\int_{r_1}^{r_2} N_{BV}\frac{dr}{r}\Big)^{-1} \tag{2.15}$$

Thus, the period spacing gives access to the integral of the N_{BV} is the Brunt-Väisälä (buoyancy) frequency weighted by the inverse of the radius, where r_1 and r_2 are the internal turning points of the gravity-mode cavity. The period spacing provides information on the central stellar regions, like distinguishing between different evolutionary stages. Essentially noticeable in red giants with an inert, or a burning helium core. Deviations from the regular period spacing pattern suggests local stellar structure changes, e.g. chemical structure changes due to the first dredge up (Hekker and Christensen-Dalsgaard, 2017).

Frequency of maximum oscillation power ν_{max} and the acoustic cut-off frequency ν_{acc}

The shape of the power excess of all solar-like oscillations together is centred around ν_{max} (Kallinger et al., 2012), the so-called *frequency of maximum oscillation power*, which is also empirically linked to the atmospheric acoustic cut-off frequency, ν_{acc}. It defines the maximum frequency at which a standing wave can occur:

$$\nu_{\mathrm{acc}} = \frac{c_s}{4\pi H_p} \tag{2.16}$$

where $\mathrm{H}_p = -(d\ln p/dr)^{-1}$ is the pressure scale height in a nearly isothermal atmosphere (Lamb, 1932). Modes are not able to propagate, when their vertical wavelength exceeds the scale of the density and pressure variations in the equilibrium structure. It is also the outer turning point, where an acoustic wave propagating outwards is reflected. A wave propagates as long as $\omega < \omega_{\mathrm{acc}}$ (Hekker and Christensen-Dalsgaard, 2017).
The frequency of maximum oscillation power ν_{max} provides a direct measure of the surface gravity g assuming the effective temperature T_{eff} is known (e.g. Brown et al. (1991), Kjeldsen and Bedding (1995)):

$$\nu_{max} \propto \nu_{acc} = \frac{c_s}{4\pi H_p} \propto \frac{g}{\sqrt{T_{\mathrm{eff}}}} \propto \frac{M}{R^2\sqrt{T_{\mathrm{eff}}}} \tag{2.17}$$

2.4.1. (Non-) linear seismic scaling relations

The global seismic scaling relations for ν_{max} and $\Delta\nu$ as in Eq. 2.17 and Eq. 2.11, respectively, can be used to estimate stellar parameters such as mass and radius in a model-independent way. This is suitable for stars providing solar-like oscillations. If scaled to the Sun, these equations become:

$$\frac{\nu_{\mathrm{max}}}{\nu_{\mathrm{max},\odot}} = \left(\frac{g}{g_\odot}\right)\left(\frac{T_{\mathrm{eff}}}{T_{\mathrm{eff},\odot}}\right)^{-\frac{1}{2}} \tag{2.18}$$

$$\frac{\Delta\nu}{\Delta\nu_\odot} = \left(\frac{M}{M_\odot}\right)^{\frac{1}{2}}\left(\frac{T_{\mathrm{eff}}}{T_{\mathrm{eff},\odot}}\right)^{-\frac{3}{2}} \tag{2.19}$$

Although these seismic relations are sufficiently accurate for main-sequence stars, they overestimate the mass and radius of red giants by about 15% and 5%, respectively. In order to adopt these relations to evolved stars, *non-linear scaling relations* based on six RGB stars, each one is part of an eclipsing binary system, and about 60 RGB and RC stars inhabited in open clusters NGC 6791 and NGC 6819, are derived:

$$\frac{g}{\sqrt{T_{\mathrm{eff}}}} = \left(\frac{\nu_{\mathrm{max}}}{\nu_{\mathrm{max},\odot}}\right)^{1.0075\pm0.0021} \tag{2.20}$$

$$\sqrt{\bar{\rho}} = \left(\frac{\Delta\nu}{\Delta\nu_\odot}\right)[\eta - (0.085 \pm 0.0025)\log^2(\Delta\nu/\Delta\nu_\odot)]^{-1} \tag{2.21}$$

The surface gravity g, the effective temperature $T_{\rm eff}$, and the mean density $\bar{\rho}$ are given in solar units, whereas $\nu_{\rm max,\odot} = 3140 \pm 5$ μHz and $\Delta\nu_{\odot} = 135.08 \pm 0.02$ μHz, and η depends on the evolutionary stage of the star, being equal to one for red giant and 1.04 ± 0.01 for red clump stars (Kallinger et al., 2018).

3. Stellar evolution in a coco-nutshell

This chapter gives an overview of stellar evolution of evolved stars, interwove in a seismic Hertzsprung-Russell diagram (HRD) for visualisation. Stellar evolution is highly mass dependent, leading to different evolutionary paths. Since in this Master's thesis only low- and intermediate-mass stars up to approximately 2.2 $M_\odot$ are involved, only these evolutionary paths are discussed. Information concerning the stellar structure and evolution, were taken from Pols (2011), Kippenhahn et al. (2012) and Lamers and Levesque (2017).

3.1. The seismic HR diagram: $\Delta\Pi_1$ - $\Delta\nu$

Oscillations in subgiants and red giants show a mixed character, allowing to probe the stellar interior. Mixed modes raise the opportunity to distinguish between different evolutionary stages, e.g., if a star is only burning hydrogen in a thin shell around its core, or if the core is burning helium simultaneously. Acoustic modes are approximately equally spaced in frequency, whereas gravity modes are equally spaced in period. The asymptotic period spacing for dipole modes $\Delta\Pi_1$ is sensitive to the density stratification in inner stellar regions (Tassoul, 1980) and provides information on the expansion of the envelope (Mosser, 2015). In combination with the large frequency separation $\Delta\nu$, which depends on the mean stellar density and provides information on the size and status of the core (Mosser, 2015), a model-independent seismic Hertzsprung-Russell diagram can be established.
Fig. 3.1 by Mosser et al. (2014) includes 1142 red giants and 36 subgiants observed by *Kepler*. Stellar masses and radii are derived from scaling relations. The following sections are accompanied by this figure.

3.1.1. Main-sequence and Schönberg-Chandrasekhar limit

During the main-sequence when hydrogen fuse into helium in the stellar core, the stars are in thermal and hydrostatic equilibrium, meaning that the nuclear energy production is outbalanced with the surface luminosity. After hydrogen-burning has ceased, stars consist of an inert helium core surrounded with a hydrogen-burning shell and a still hydrogen-rich envelope. The stellar core can only maintain hydrostatic and thermal equilibrium, and withstand the pressure of the overlying layers, if the isothermal, non-degenerate core with a relative maximum core mass fraction $q_c = M_c/M$ does not exceed the Schönberg-Chandrasekhar (SC) limit (Schönberg and Chandrasekhar, 1942):

$$\frac{M_c}{M} < q_{\rm sc} = 0.37\Big(\frac{\mu_{\rm env}}{\mu_c}\Big)^2 \approx 0.10 \tag{3.1}$$

where μ_c and μ_{env} are the mean molecular weight in the core and in the envelope, respectively. Depending on the stellar mass, stars follow different evolutionary tracks. Low-mass stars (0.8 $M_\odot$ up to ≈ 2 $M_\odot$) develop a degenerate helium core, which keeps the core almost isothermal and acts as an additional pressure support against the weight of the envelope. In this case the SC-limit no longer applies. In intermediate-mass stars (2 $M_\odot$ up to ≈ 8 $M_\odot$), the ashes of the hydrogen-burning shell add mass to the helium core, leading to its growth in mass. When the core mass exceeds the SC-limit, thermal equilibrium is no longer possible, the core contracts and a temperature gradient develops. The temperature and pressure gradient need to balance the gravitational force to keep the star in hydrostatic equilibrium.

3.1.2. Giant evolution

Subgiants

After hydrogen is exhausted in the core, a star exits the main-sequence and enters the subgiant stage. Its dense radiative core contracts quasi-static on a thermal timescale, while the envelope expands according to the *mirror principle*, stating that if the core contracts the envelope must expand and vice versa in order to maintain thermal equilibrium. While intermediate-mass stars undergo a rapid phase of *thick-* and *thin-shell burning* across the Hertzsprung-Russel diagram, low-mass stars experience a gradual transition. Along the subgiant evolution, the stellar radius increases whereas the mean stellar density, thus $\Delta\nu$, decreases. Due to the contraction of the radiative core, the period spacing $\Delta\Pi_1$ decreases as well. This decline in density from subgiants to red giants can be clearly followed in Fig. 3.1. When both types settle on the bottom of the *red giant branch*, they consist of a deep convective envelope on top of a relatively small radiative zone, a thin hydrogen-burning shell and an inert (and degenerate; for low-mass stars) helium core.

Red giant branch

On the red giant branch, low-mass stars are dominated by their degenerate helium core. The degeneracy causes pressure and temperature to decouple, leading to no significant increase in temperature. The core mass slowly increases due to the helium produced by the burning hydrogen shell. Caused by the degeneracy of the core, an increase in core mass results in contraction and heating of the inert helium core, whereas the shell increases its energy production, and thus its luminosity. The density and pressure gradient between the core and the envelope becomes so large that the two are basically decoupled and the stellar structure almost entirely depends on properties of the inert, degenerate helium core. The core contracts along the red giant branch, hence the core density increases but $\Delta\Pi_1$ decreases (Mosser et al., 2012b). In the diagram, the transition from the subgiant to the red giant phase is almost independent of the stars' initial conditions (e.g. mass, metallicity), suggesting that all low-mass stars with the same core structure have the same mean density (Mosser et al., 2014).
When it comes to the *first dredge-up*, the convective envelope penetrates so deep into the

stellar interior, that the remaining chemical products of the nuclear fusion during the main-sequence are transported up to the surface. The surface helium abundance increases, while the hydrogen abundance decreases, so does the carbon/nitrogen ratio. During the evolution on the red giant branch, low mass stars also suffer from mass loss. As the radius of the star and the luminosity increases, the envelope becomes loosely bound, and the large photon flux removes mass from the stellar surface. When the star reaches the top of the red giant branch, the temperature in the core is high enough to ignite helium, i.e. at a temperature of $\sim 10^8$ K at a core mass of $\sim 0.45\ M_\odot$. Due to the strong degeneracy of the core, helium ignition is an unstable process, and leads to a thermonuclear runaway, the so-called *helium flash*. This immense overproduction of nuclear energy happens on a very short timescale of the order of a few hours and is absorbed by the expansion of the non-degenerate layers above the core. Helium flashes are an artefact of stellar models. Up to now, there is no observational confirmation of them in real stars.
Low-mass stars located in Fig. 3.1 at low $\Delta\nu$ and an unusually high $\Delta\Pi_1$ contain a small radiative region, which could match a helium subflash. Stellar models would predict several such subflashes after the first helium flash, where each one is located closer to the centre until the degeneracy in the core is completely lifted, leaving a star in equilibrium with a convective helium burning core. After the helium flash, the energy production of the shell is diminished. This leads to a decrease in luminosity while the envelope contracts and the core expands. When the star has restored hydrostatic equilibrium, it settles in the *red clump* with an increased $\Delta\Pi_1$.
Along with low-mass stars, intermediate mass stars experience the *first dredge-up*, changing the chemical composition at the stellar surface, while in the meantime, the core proceeds contracting and heating. At the tip of the red giant branch, when the conditions are satisfied, a gentle helium ignition takes place due to the non-degenerate core, which causes nuclear burning to be thermally stable. These stars settle in the *secondary red clump*.

Red Clump and Horizontal Branch

The stellar interior inhabits at this point of evolution two energy sources, namely the helium-burning core, producing carbon and oxygen via the *triple-alpha process*, surrounded by the hydrogen-burning shell. At the beginning of helium-burning, the core increases in mass and expands, while the envelope contracts, leading to a decrease in luminosity and an increase of $\Delta\Pi_1$ and $\Delta\nu$. Although there is an additional fusion in the core, the shell generates less energy, but is still the main source of energy generation in the star. Somewhat later, $\Delta\Pi_1$ and $\Delta\nu$ decrease because the energy production gets less efficient. Stars with approximately solar metallicity settle in the red clump, while stars with lower metallicity settle on the *horizontal branch*. Both types form a compact region in the HR diagram because the core mass was roughly the same at the time of core helium ignition. There is only a slight dependence of the envelope mass, thus radius and effective temperature may vary from star to star.
Red clump stars form a dense and small region around $\Delta\Pi_1 \simeq 300$ s and $\Delta\nu \simeq 4.1\ \mu$Hz. They have similar core masses, hence similar luminosities. Low-mass red clump stars have lower $\Delta\nu$ than the slightly more massive red clump stars, thus lower mean density.

Secondary Clump

In the secondary clump, stars fuse helium into carbon and oxygen via the highly temperature sensitive triple alpha (3α) process, giving rise to a growing convective core. The hydrogen-burning shell contributes most to the energy output of the star, while for the core only a small release of energy is adequate to outbalance its energy loss and prevent the core from contracting. Due to the different core masses at the time of gradual helium ignition, the stars form the secondary clump at lower luminosities and effective temperatures than the red clump stars. In Fig. 3.1, the secondary clump stars occupy a widespread region where on one side $\Delta\Pi_1$ decreases with increasing stellar mass up to $\sim 2.7\ M_\odot$, and on the other side for masses above $\sim 2.8\ M_\odot$, $\Delta\Pi_1$ increases with mass.
An additional effect established with detailed stellar evolution models are *loops* in the HR diagram. During core helium burning, the star loops across the HR diagram, induced by its central chemical composition profile during core hydrogen-burning on the main-sequence. The extension of its loop increases with increasing stellar mass. At the apex of the loop, the star has its minimum stellar radius and local maximum effective temperature, subsequently the envelope starts expanding, and the star moves back to its starting position.

Asymptotic giant branch

In stars located in the vicinity of the red clump with smaller period spacing, the core is contracting because helium gets gradually depleted. These stars prepare to ascend the asymptotic giant branch. After helium is exhausted, an inert carbon-oxygen core surrounded by a helium shell and a hydrogen shell where burning takes place. The helium-burning shell adds gradually mass to the growing CO-core, resulting in an increase in density, and thus the core becomes degenerate. Only stars with masses $4 - 8M_\odot$ with an extinguished hydrogen-burning shell experience the *second dredge-up*. This allows the convective envelope to reach deep into the helium-rich layers. The products of fusing hydrogen and helium, e.g., carbon, oxygen, nitrogen, and helium, are transported to the surface of the star. This secondary dredge-up does not occur in low-mass star because their hydrogen-shell is still active at low level. Thus, the envelope cannot penetrate any further than the hydrogen-shell into the star.
After the hydrogen-shell is reignited due to the decrease in luminosity, resulting in contraction of the layers above, a phase of *double shell burning* begins. During that time, the shells do not fuse at the same pace, thus the helium-burning shell becomes thermally unstable and causes a *helium shell flash*. Stars that do not ignite carbon in their core go through a series of *thermal pulses* during the AGB evolution, until most of their envelope is lost. The star then becomes the centre of a planetary nebula, where the interaction of winds forms a dense, optically thin shell from which radiation is emitted. Finally, if the envelope mass is less than 5 % of the total mass, the envelope contracts, the hydrogen shell burning is extinguished, and a degenerate CO core is left. The stellar remnant has evolved to a *white dwarf*.

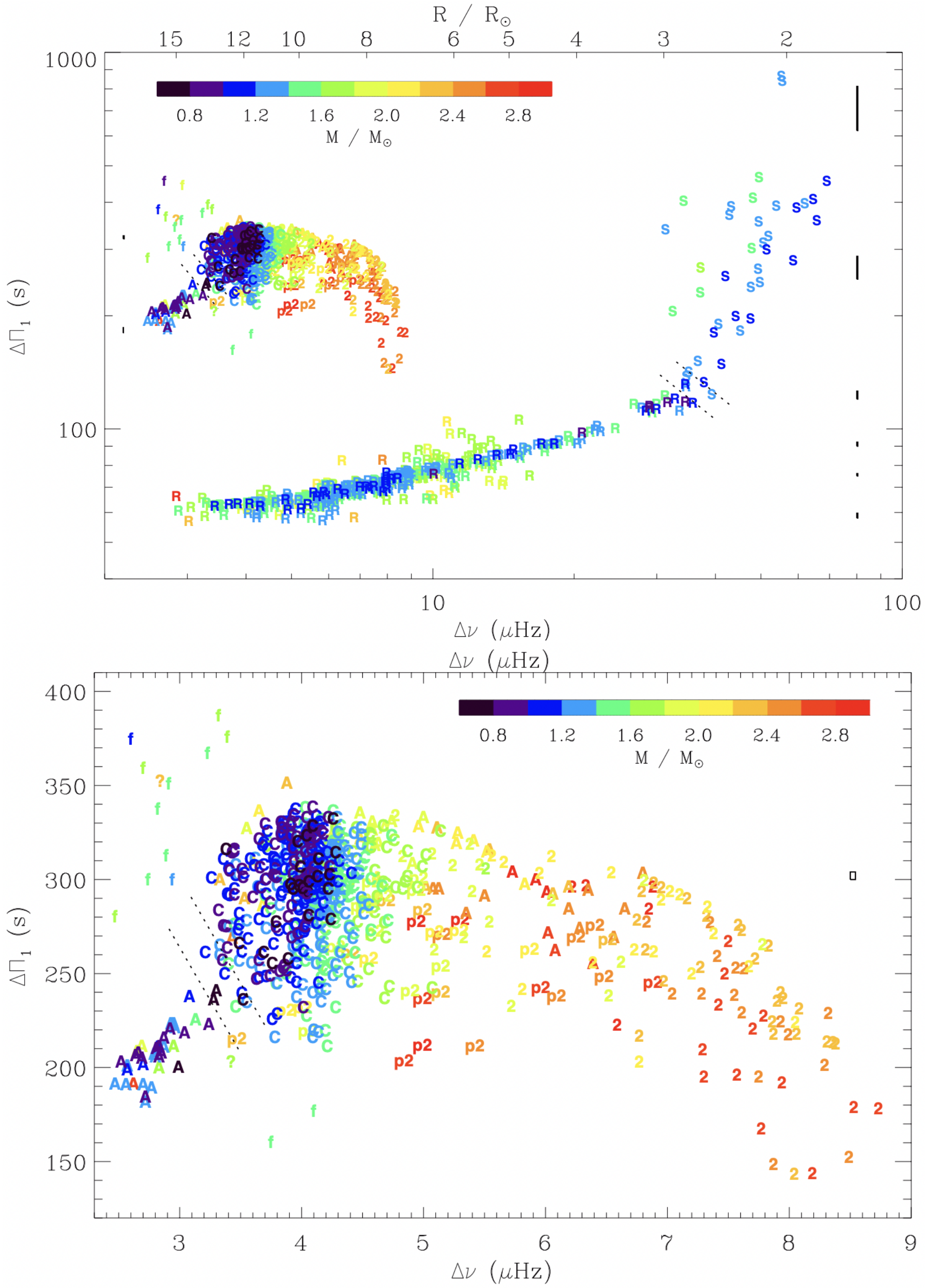

Figure 3.1.: Period Spacing $\Delta\Pi_1$ as a function of the large separation $\Delta\nu$ resulting in a seismic HRD. The different evolutionary stages are as follows: subgaints (**S**), red giants (**R**), helium subflash stage (**f**), red clump (**c**), pre secondary clump (**2**), secondary clump (**2**), and stars evolving towards the asymptotic giant branch (**A**). The colour coding shows a proxy of the seismic stellar mass. The dotted lines show the approximate transitions between the evolutionary stages. *Bottom*: zoom on the red clump. Figure taken from Mosser et al. (2014).

4. Stellar Rotation

It is plausible that all stars rotate because the molecular cloud responsible for a star to form contains angular momentum (Hekker and Christensen-Dalsgaard, 2017). Rotation impacts the stellar structure by perturbing the hydrostatic equilibrium, as well as the transport of angular momentum and chemical composition. There are several processes that are potentially capable of transporting angular momentum in stars: hydrodynamical instabilities, and meridional circulation, internal gravity waves and magnetic fields (Deheuvels et al., 2015).
In stellar evolution codes, the modelling of hydrodynamical transport processes is challenging when rotation and mixing are included. For example, purely hydrodynamical mechanisms that transport angular momentum do not sufficiently reproduce the direct observations of internal stellar properties obtained by rotational splittings of red giants (Deheuvels et al., 2020). There has not yet been found a satisfying solution to match angular momentum transport in stellar evolution codes. Thus, current observations still raise many questions.

4.1. During subgiant evolution

The investigation of the internal rotation of less evolved subgiants is essential to understand the transition between the nearly uniform rotating main-sequence stars and the angular momentum gradient observed on the bottom of the red giant branch. However, the oscillation spectra of young subgiants contain only few g-m modes to probe the internal rotation. This challenges its extraction as the core of subgiants is less dense, hence the Brunt-Väisälä frequency is lower, and so are the frequencies of their gravity modes. Subgiants have g modes at low radial order (n $\sim$ 1), whereas typical red giants branch stars have g modes at high radial order (n $\sim$ 100) (Mosser et al., 2012b). Furthermore, pressure modes are coupled with the lowest-order gravity modes resulting in a large frequency separation between consecutive g modes, and thus the oscillation spectra contain only few g-m modes. Another important point is that subgiants have a higher effective temperature than red giants, which effects the damping of the oscillation modes (Deheuvels et al., 2020). As the mode lifetime is the reciprocal of the damping rate ($\tau = 1/\eta$), oscillation modes of subgiants have a shorter lifetime and thus larger linewidths ($\Gamma = 1/\pi\tau$) in the oscillation spectra (Hekker and Christensen-Dalsgaard, 2017). Large linewidths can cover rotational splittings, making them hard to disentangle. Finally, the excited modes in subgiants have frequencies well above the *Nyquist* frequency ($\sim$ 283.5 μHz) of the long-cadence data of *Kepler* but gladly the short-cadence data can be used with a Nyquist frequency well above 8 mHz. The Nyquist frequency ($\nu_{\rm Nyq} = \frac{1}{2\Delta t}$, with Δt being the

sampling rate in case of evenly sampled timeseries) is the hard limit up to which useful signal can be extracted from an amplitude spectrum (Eyer and Bartholdi, 1999).
Keeping the limits above in mind, Deheuvels et al. (2020) and Deheuvels et al. (2014) investigated the mean core and envelope rotation rates of subgiants and a young red giant by using rotation inversions and found interesting results in Tab. 4.1 and Fig. 4.1. The youngest two subgiants from Deheuvels et al. (2020) are nearly consistent with a solid-body rotation within the entire interior. There has to occur an efficient transport of angular momentum to execute a nearly solid-body rotation. The six slightly more evolved subgiants and the young red giant, investigated by Deheuvels et al. (2014), show a clear increasing trend during the subgiant branch evolution. The mean core rotation rate thus appears to be correlated with evolution. These findings show that the core of subgiants spins up until the star reaches the bottom of the red giant branch, where the core rotation brakes (e.g. (Gehan et al., 2018), (Mosser et al., 2012a)) caused by a yet unknown mechanism redistributing angular momentum from the core up to the envelope. During the subgiant phase, the angular momentum transport thus seems to be rather insufficient to counterbalance the core contraction, resulting in an acceleration of the core in this phase.

4.2. Along the red giant branch

Following stellar evolution, we are now settled at the base of the red giant branch. The central region of the core contracts and heats, while the outer envelope expands and cools. The star evolves to a red giant, where convection takes over a large mass fraction of the star. Under the assumption of angular momentum conservation, the core is required to rotate faster than its envelope. Beck et al. (2012) investigated the internal rotation of three low-luminosity *Kepler* red giants in their early phase of hydrogen-shell burning by analysing the rotational splitting of mixed modes. It was found by comparing the observed rotational splittings with a theoretical stellar model containing non-rigid rotation, that the core rotates approximately ten times faster than the surface, leading to a strong differential rotation. Interestingly, in models of angular momentum evolution, the core rotation rate is still overestimated and does not match the slower core rotation rate of real red giants. Therefore, a still unknown process must be at work, transferring angular momentum from the core into the envelope.
At this point the analysis, *Kepler* raises the opportunity for large studies to constrain the internal stellar rotation. The first one to begin with was Mosser et al. (2012a) who probed the rotational splittings of about 300 red giants in the early stages of the red giant branch, in the red clump, and secondary red clump. Their results suggest that the stellar core has to spin down, when the giants ascend the red giant branch. Thus, angular momentum is transferred from the core to the envelope to spin down the core. The observed mean core rotation period is larger for clump stars than for red giant branch stars, which requires a redistribution of angular momentum to spin down the core along stellar evolution, indicating a strong differential rotation (Mosser et al., 2012a).
Gehan et al. (2018) refined the results obtained by Mosser et al. (2012a) by identifying the

Deheuvels et al. (2020)

Star	$\langle\Omega\rangle_g/(2\pi)$	$\langle\Omega\rangle_p/(2\pi)$	$\langle\Omega\rangle_g/\langle\Omega\rangle_p$
KIC 8524425	204 ± 134	288 ± 20	0.68 ± 0.47
KIC 5955122	488 ± 227	675 ± 27	0.72 ± 0.37

Deheuvels et al. (2014)

Star	$\langle\Omega\rangle_g/(2\pi)$	$\langle\Omega\rangle_p/(2\pi)$	$\langle\Omega\rangle_g/\langle\Omega\rangle_p$
KIC 12508433	532 ± 79	213 ± 26	2.5 ± 0.7
KIC 8702606	629 ± 109	164 ± 17	3.8 ± 1.1
KIC 5689820	865 ± 35	125 ± 13	6.9 ± 1.0
KIC 8751420	1540 ± 50	102 ± 24	15.1 ± 4.0
KIC 7799349	1313 ± 26	122 ± 15	10.7 ± 1.5
KIC 9574283	1556 ± 22	74 ± 28	21.0 ± 8.2

Deheuvels et al. (2012)

Star	$\langle\Omega\rangle_g/(2\pi)$	$\langle\Omega\rangle_p/(2\pi)$	$\langle\Omega\rangle_g/\langle\Omega\rangle_p$
KIC 7341231	710 ± 51	$<$ 150 ± 19	4.73

Deheuvels et al. (2015)

Star	$\langle\Omega\rangle_g/(2\pi)$	$\langle\Omega\rangle_p/(2\pi)$	$\langle\Omega\rangle_g/\langle\Omega\rangle_p$
KIC 8962923	138 ± 8	79 ± 10	1.8 ± 0.3
KIC 5184199	200 ± 13	63 ± 20	3.2 ± 1.0
KIC 4659821	165 ± 14	79 ± 15	2.1 ± 0.4
KIC 3744681	194 ± 20	63 ± 36	3.1 ± 1.8
KIC 7467630	121 ± 18	96 ± 28	1.3 ± 0.4
KIC 9346602	164 ± 6	53 ± 15	3.1 ± 0.9
KIC 7581399	167 ± 11	84 ± 14	2.0 ± 0.4

Table 4.1.: All values are given in nHz. $\langle\Omega\rangle_g$ represents the mean rotation rate over the g-mode cavity, whereas $\langle\Omega\rangle_p$ is the mean rotation rate in the p-mode cavity, which is an upper limit of the rotation rate of the convective envelope. The different phases of stellar evolution, showing young subgiants from Deheuvels et al. (2020) and Deheuvels et al. (2012), followed by subgiants and an early red giant from Deheuvels et al. (2014) and secondary clump stars from Deheuvels et al. (2015).

rotational multiplet components and estimating the mean core rotation measurements for 875 *Kepler* red giant branch stars for various mass ranges from 1 to 2.5 $M_\odot$. Gehan et al. (2018) rather suggests, due to the low core rotation rates at the lower red giant branch, an almost constant core rotation along the red giant branch than an actual slow down. In addition to that, the evolving core rotation along the red giant is mass independent.

However, in this case the yet unknown physical mechanism counterbalances core contraction along the red giant branch, as contraction should cause an acceleration in the core rotation unless angular momentum is redistributed in the stellar interior. The timescale on which stellar evolution occurs is mass-dependent, thus mechanisms that transport angular momentum at distinct efficiency must exist to maintain a rather constant core rotation along the red giant branch.

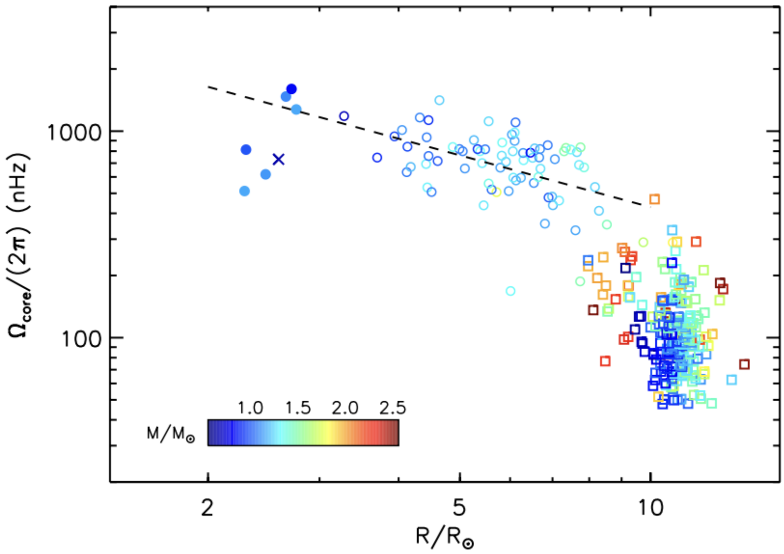

Figure 4.1.: Core rotational rate as a function of stellar radius. The 6 filled symbols show measurements for subgiants Deheuvels et al. (2014), the cross is the early red giant from Deheuvels et al. (2012), while the open symbols present the data obtained by Mosser et al. (2012a) for red giant branch stars (circles) and red clump stars (rectangles). The colour-coding gives the mass range. Figure taken from Deheuvels et al. (2014).

4.3. In the clump

The determination of the rotational splittings to estimate the amount of internal radial differential rotation for secondary clump stars is again challenging. First, one must keep in mind that helium-burning via 3α process occurs in a very small convective core where gravity waves cannot propagate, thus the rotation rates are limited to layers around the convective core. To select suitable targets with modes clearly split by rotation in the power spectra, one must differentiate between red giants and red clump stars, which is rather challenging since the mode lifetimes are shorter, and thus provide larger widths than red giant branch stars. Furthermore, the longer rotation periods of clump stars result in smaller rotational splittings compared to red giant branch stars. Clump stars therefore often show mode widths similar to rotational splittings, which can cause complications for

identifying p-m modes but not for g-m modes providing larger inertia, and thus shorter widths.
After the main sequence, intermediate-mass stars evolve rather quickly towards the secondary clump, which raises the question if angular momentum transport can operate on a Kelvin-Helmholtz timescale. If this is not the case, these stars would provide a strong differential rotation, including a very fast spinning core. But the opposite was found by Deheuvels et al. (2015) who investigated the rotational splittings of mixed modes in seven helium burning intermediate-mass secondary clump stars observed by *Kepler*. The p-dominated and g-dominated mixed modes show a comparable rotational splitting for secondary clump stars, which differs greatly with what was observed by Mosser et al. (2012a) for red giant branch stars, namely that g-m modes have about twice the splitting of p-m modes. This suggests less differential rotation in secondary clump stars than in red giant branch stars. Deheuvels et al. (2015) found a core-to-envelope ratio ranging from 1.8 ± 0.3 to 3.2 ± 1.0 showing a weaker radial differential rotation for secondary clump stars than for red giant branch stars. Solid-body rotation was as well be ruled out for the six out of seven stars, where one shows only marginally a solid-body rotation profile.
The weak radial differential rotation found points towards a very efficient angular momentum redistribution. If the redistribution occurs before helium is ignited in the core, it must happen on a very short timescale. Assuming the same mechanism is responsible for transporting angular momentum for low- and intermediate mass stars, it must happen on a thermal timescale.

5. Data

5.1. An observational history

The journey starts in the early 1960s when Leighton et al. (1962) first discovered oscillations in the Sun obtained from ground-based radial-velocity observations via Doppler difference plates, suggesting a period T of 296 $\pm$ 3 s and a velocity amplitude A of 0.4 km/s and a mean lifetime τ of approximately 380 s. Since then, scientist have been curious to find p modes at the stellar surface in other stars than the Sun. Finally, in the early 1990s, oscillations were first confirmed and detected in Procyon B by Brown et al. (1991). At that time, it was challenging to detect solar-like oscillations due to their extremely small pulsation amplitudes. The improving precision of ground-based radial velocity measurements for detecting exoplanets increases the data pool for asteroseismic analysis. This was the beginning of a series of detection of stochastically driven oscillations in other main-sequence stars, subgiants, and also red giants. The advent of space-based photometric observations like the Canadian microsatellite MOST[1] (**M**icrovariability and **O**scillations in **ST**ars, launched in 2003), which was entirely dedicated to stellar pulsations, extended the scientific outcome. With MOST, evidence for non-radial mixed modes in red giant HD 20884 was found by Kallinger et al. (2008). The major breakthrough, which revolutionized asteroseismic research was CoRoT[2] (**Co**nvection **Ro**tation and planetary **T**ransists, launched 2006). CoRoT detected oscillations in certain main sequence stars and several thousands of red giant stars. Additionally, with CoRoT it was unambiguously determined by investigating a sample of over 300 red giants, that red giants oscillate in radial and non-radial modes (De Ridder et al., 2009), which raises the opportunity to probe the internal structure of red giants. The *Kepler*[3] space telescope extended the sample of asteroseismic targets towards low-mass stars, which resulted in the detection of over 500 main-sequence stars and over 20.000 red giants. An illustration of the number of detected oscillations can be seen in Fig. 5.1.

5.1.1. The NASA Kepler and K2 mission

The *Kepler Space telescope* launched in March 2009 performed high-precision photometry with a 0.95 m aperture and a 105 square deg field-of-view (FOV). The photometer is composed of an array of 42 charge coupled devices (CCD), where each 50×25 mm CCD has 2200×1024 pixels. Kepler performed time-series observations, or measured light-curves

[1] `https://astro-canada.ca/le_telescope_spatial_most-the_most_space_telescope-eng`
[2] `https://corot.cnes.fr/en/COROT/index.htm`
[3] `https://www.nasa.gov/mission_pages/kepler/overview/index.html`

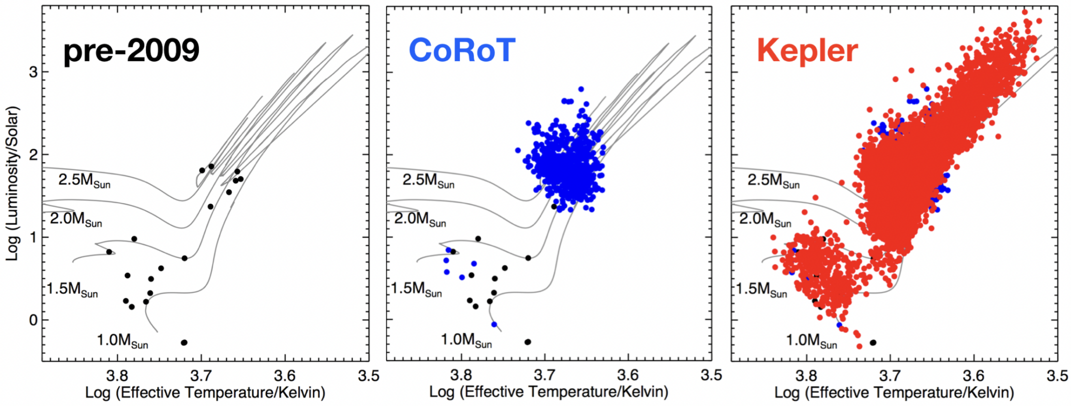

Figure 5.1.: HRD displaying stars where solar-like oscillations had been detected prior to 2009 (left panel, ∼ 20), with CoRoT (middle panel, several thousand), and *Kepler* (left panel, over 20.000). The solid lines show evolutionary tracks with distinct masses. Taken from Huber and Zwintz (2020).

in long-cadence (30 min) for approximately 170.000 stars and in short-cadence (1 min) for 512 stars. The mission goal was primarily to search and characterize habitable planets ($\geq$ 1 $R_\oplus$) orbiting sun-like stars. To observe transits, it is necessary that the planet's orbit is aligned along the line of sight to the spacecraft. As this is rather unlikely, Kepler needed to monitor at least 100.000 stars at once. In May 2013, after about 4 years operation time, Kepler suffered a failure on its reaction wheels responsible for the pointing ability. This misfortune led to the NASA K2 mission. It was designed to survey the ecliptic, with the science goal to discover exoplanets in nearby low-mass faint red giants and close bright stars. Additionally, it also used the advantage of its ecliptic pointing to observe bright open clusters, star-forming regions towards the galactic centre, red giants across the galaxy, extragalactic and solar system objects, supernovae, and microlensing events. The mission became fully operational in May 2014, and lasted as long as possible, until the spacecraft run out of fuel by the end of October in 2018. It was shut down two weeks later (Howell, 2020).

Overall, the scientific results obtained from the NASA Kepler and K2 mission were astonishing and have still an important impact on many areas of astrophysics.

5.2. Data

For this Master's thesis, a data set of 6179 red giants obtained by the Kepler mission at different evolutionary stages from the bottom of the red giant branch up to the asymptotic giant branch was provided. The red giants are part of the second release of the *Apache Point Observatory Kepler Asteroseismology Science Consortium (APOKASC)*. Stellar properties were achieved by analyzing the *Apache Point Observatory Galactic Evolution*

Experiment (APOGEE) spectroscopic parameters in combination with the asteroseismic data obtained from the Kepler mission (Pinsonneault et al., 2018)
Kallinger (2019) extracted at least three radial orders for these mentioned stars, including

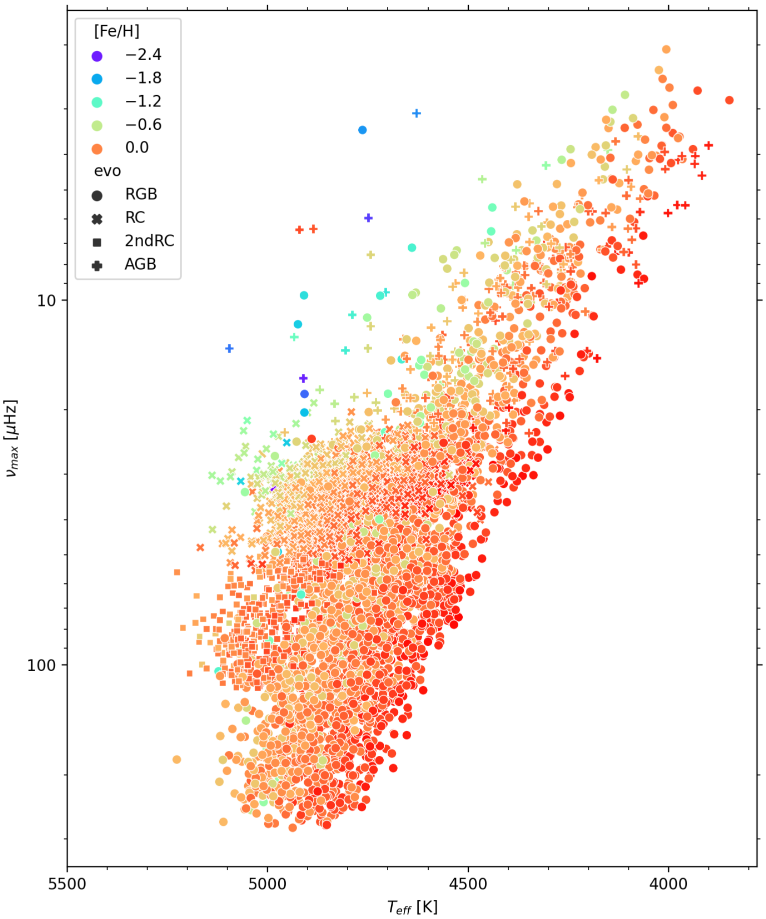

Figure 5.2.: Full sample of 6179 red giants positioned in a seismic HR diagram for visualisation. The colour-coding depicts the distinct metallicities whereas the different symbols aim to the specific evolutionary stage. Data has been taken from APOKASC (Pinsonneault et al., 2018).

mode parameters of individual frequencies for more than 250.000 oscillation modes of spherical degree l = 0 to 3 by applying the *'Automated Bayesian Peak-Bagging Algorithm'* (AꓭBA). This method is quite challenging due to the multitude of non-radial mixed modes in-between radial pressure modes, as this can include more than ten dipole mixed modes. In addition to that, rotation causes the modes to split into duplets or triplets, which enhances the number of frequencies in the *power density spectra, PDS*. Table 5.1 gives an overview of the count of distinct spherical degrees in combination with their evolutionary stage. The output of AᗺBA for each analyzed star contains general

evo.	# of stars	l = 0	l = 1	l = 2	l = 3	Σ
RGB	3375	24138	89162	21592	5493	140385
RC	2121	14490	65882	12967	1353	94692
2^{nd} RC	448	3776	13063	3578	440	20857
AGB	235	1092	642	1113	0	2847
Σ	6179	43496	168749	39250	7286	258781

Table 5.1.: Total number of stars and the extracted modes at different evolutionary stages including spherical degree l = 0 to 3.

information in the header as well as the individual mode parameters listed in the Tab. 5.2 below. The full extent of échelle diagrams, mode files, and PDS are available on `https://github.com/tkallinger/KeplerRGpeakbagging`.

Header information	
f_{max}	frequency of maximum oscillation power ν_{max}
$\Delta\nu$, $\delta\nu_{02}$, f_c	large and small frequency separation via the three central radial order around ν_{max}, and the central radial mode frequency
$\Delta\nu_{cor}$, α	dimensionless curvature parameter including corrected large separation
evo	evolutionary stage: RGB → 0, RC → 1, 2^{nd} RC → 2 and AGB → 3

Mode parameters	
l	spherical degree
freq	mode frequency
amp	root-mean-square amplitude in parts per million
τ	mode lifetime in days
ev, ev1	evidence of the mode; ev1 is valid for dipole modes

Table 5.2.: Output parameters of AᗺBA, in μHz otherwise stated separately.

6. Method

Mixed dipole modes as a key to internal rotation

Mixed modes consist of a coupling between pressure modes from the outer acoustic cavity and gravity modes propagating in the radiative interior of the star (Scuflaire, 1974). Depending on the dominant amount of either pressure or gravity properties, they are called pressure-dominated mixed modes (*p-m modes*) or gravity-dominated mixed modes (*g-m modes*), respectively. Dipole mixed modes are found in so-called *dipole forests* between consecutive radial modes where the p-m modes are situated around the theoretical pure pressure mode, which is approximately situated in the middle between two consecutive radial modes, providing a large amplitude in the envelope but a low mode inertia. Gravity-dominated mixed modes are subsequently situated rather close to a radial order, i.e. close to $l = 0$ and 2 modes, leading to a small amplitude in the core but a high mode inertia (e.g. Dupret et al. (2009)). These dipole mixed modes are of special interest because they are most frequent in the spectrum (e.g. Table 5.1), do hardly suffer from partial cancellation (Aerts et al., 2010), and in the case of rotational splittings, dipole mixed modes are split into a maximum of three components (2l+1) depending on the inclination i of the star. For a star seen pole-on, *singlets* with $m = \{0\}$ are expected, whereas a star seen equator-on only shows the wing components (a *duplet*) with $m = \{+1, -1\}$ in the power spectra. For an intermediate inclination *triplets* are expected with $m = \{+1, 0, -1\}$. Within a rotational multiplet, the mixed modes are assumed to have a common width. Whereas, the heights of the modes can be different, depending on the mode inertia (Dupret et al., 2009). This frequency separation between each part of the multiplet reveals information on the angular velocity and the propagation region of the mode (Beck et al., 2012). The observed rotational splittings are not constant throughout the dipole spectrum. The lowest value is found for the rotational multiplet situated nigh the pure pressure mode, while the highest value is found in the wings (e.g. Beck et al. (2012), Mosser et al. (2012a))

6.1. Choosing targets

Clearly not all stars in this sample are suitable to provide the necessary amount of information for good results, thus some boundary conditions are set beforehand. For various frequencies the mode evidence is below the threshold of 0.91, i.e., the probability that the mode is reliable and not due to noise. It would have been a preferred step to only consider modes above this threshold. Following this approach unfortunately lead to rather unclear histograms, which in turn challenges the detection of the guessed rotational splitting. Accordingly, the whole range of mode evidence is used for analysis. The only

prior condition applied was to probe only stars that provide at least 8 dipole mixed modes to become a minimal count of potential multiplets. This reduces the total sample of 6179 stars to 4963 stars at distinct evolutionary stages.
The evolutionary history is displayed in the internal structure of evolved stars. The g-m mode inertia increases along the red giant branch causing less visible mixed modes and increases the challenge of identifying the split-components (e.g. Gehan et al. (2018), Dupret et al. (2009)). Therefore, the already reduced sample will again reduce itself during the workflow. At the beginning, the sample is distributed as shown in Tab. 6.1.

evo	# of stars
RGB	1605
RC	678
2^{nd} RC	274
AGB	19
Σ	2576

Table 6.1.: Reduced sample divided into the various evolutionary stages containing at least 8 dipole mixed modes.

6.2. Modulation of the rotational splittings

According to Mosser et al. (2012b), the rotational splitting can be written as:

$$\delta\nu_{split} = \nu_{n,1,m} - \nu_{n,1} = m\mathcal{R}\delta\nu_{rot} \tag{6.1}$$

where m is the azimuthal order, $\mathcal{R}$ is the rotation profile, and $\delta\nu_{rot}$ is the maximum observed splitting for g-m modes. Basically, the rotational splitting $\delta\nu_{\mathrm{split}}$ is the separation in frequency between the non-rotating, central frequency of dipole modes $\nu_{\mathrm{n,1}}$ and two wing components $\nu_{\mathrm{n,1,m}}$. Between two consecutive radial modes lies the theoretical pure p-mode ν_{p_1} surrounded by p-m modes, which can be very close but still providing a significant g-mode contribution. In contrast, g-m modes are situated further outward, close to the radial modes. Empirically, this behaviour follows a Lorentzian function:

$$\mathcal{R}_{n_p}(\nu) = 1 - \frac{\lambda}{1 + \left(\frac{\nu - \nu_{n_p,1}}{\beta\Delta\nu}\right)^2} \tag{6.2}$$

The terms λ and β are frequency independent and empirically determined to have values close to 0.44 and 0.05, respectively (see Fig. 7.3). For the theoretical pure p-mode frequency a simple approach is used, by taking the mean frequency between two consecutive radial modes as an approximation.

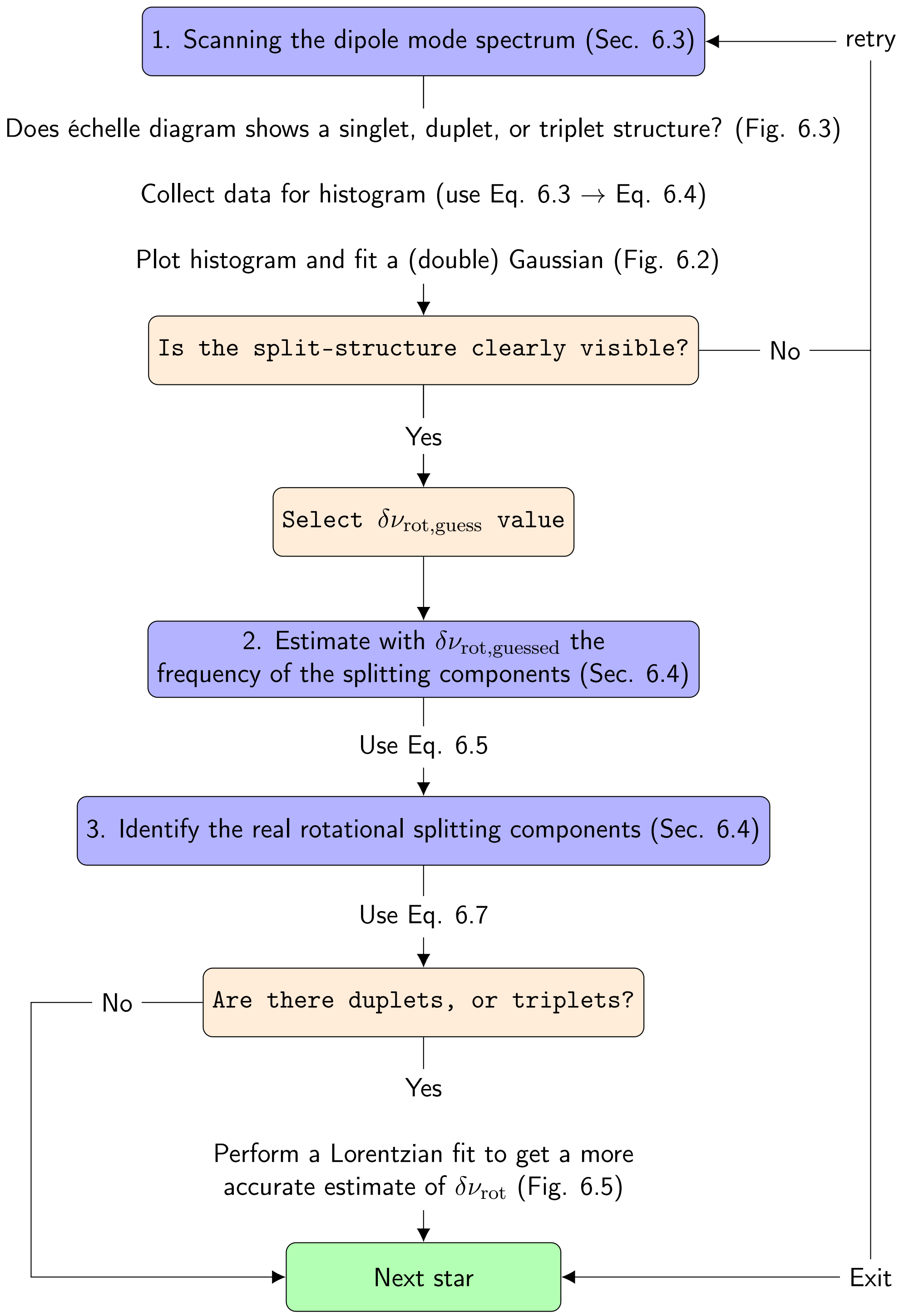

Figure 6.1.: Flow chart of the required steps within the code.

6.3. Scanning the dipole mode spectrum

The theoretical description of the elaboration of the code is guided by Fig. 6.1, while the full extent of the code is given in Appendix A.

The first step was to create an automated way to scan the power density spectrum to find the most frequent splitting, as the split components share roughly a common width. Furthermore, the splittings of dipole g-m modes do in first proximity do not vary from one radial order to another. This allows a continuous scan throughout the spectrum. Rotational splittings of g-m modes provide a measure for the rotation averaged over the central region. To get a first guess of the rotational splitting $\delta\nu_{\text{split,guess}}$, a statistical approach was performed. The scan starts with the first dipole mode at lowest frequency ν_j for $j = (0, \dots, N)$, where N is the total count of available dipole modes of the star. The frequency separation $\Delta\nu_{j,j+i}$ between ν_j and the frequency ν_{j+i} for $i = (1, 4]$ is calculated, and inserted into the rearranged form of the rotation profile $\mathcal{R}_{n_p}$ Eq. 6.4 to build a histogram for $\delta\nu_{\text{rot,guess}}$.

$$\begin{aligned}
\Delta\nu_{j,j+i} &= |\nu_j - \nu_{j+i}| \rightarrow \delta\nu_{\text{split,guess}} \\
&= |\nu_0 - \nu_{0+1}| \rightarrow \delta\nu_{\text{split,guess}} \\
&= |\nu_0 - \nu_{0+2}| \rightarrow \delta\nu_{\text{split,guess}} \\
&= |\nu_0 - \nu_{0+3}| \rightarrow \delta\nu_{\text{split,guess}} \\
&= |\nu_0 - \nu_{0+4}| \rightarrow \delta\nu_{\text{split,guess}} \\
&= |\nu_1 - \nu_{1+1}| \rightarrow \delta\nu_{\text{split,guess}} \\
&= |\nu_1 - \nu_{1+2}| \rightarrow \delta\nu_{\text{split,guess}} \\
&= \qquad \vdots
\end{aligned} \tag{6.3}$$

$$\delta\nu_{\text{rot,guess}} = \delta\nu_{\text{split,guess}} \left(1 - \frac{\lambda}{1 + \left(\frac{\nu - \nu_{\text{p},1}}{\beta\Delta\nu}\right)^2} \right)^{-1} \tag{6.4}$$

The frequency ν_{j+i} is iterated four times, while the origin frequency ν_j is still consistent. The step size of four was chosen to identify triplets. After that, the ν_j is shifted to the next one at ν_{j+1} proceeding with the loop.
Slight random normal distributed variations of λ and β are used to improve the histogram, and the visibility of the peaks therein, as well as the empirical condition that the guessed split must be smaller than a sixth of the large separation. This boundary was chosen because the rotational splitting of red giants does not exceed this limit. For example, it is assumed for a red giant with $\Delta\nu \approx 18$ that its $\delta\nu_{\text{split}} < 1\ \mu$Hz, thus $\frac{\Delta\nu}{6} \approx 3\mu$Hz can assist as an upper border.
The resulting histogram seen in Fig. 6.2 shows the distribution of the guessed rotational splittings, fitted with a double Gaussian normal distribution performed with the *UltraNest*

software package. The posterior probability distributions and the Bayesian evidence were derived with the nested sampling Monte Carlo algorithm *MLFriends* (Buchner (2016), Buchner (2019)) using the UltraNest[1] package (Buchner (2021)).

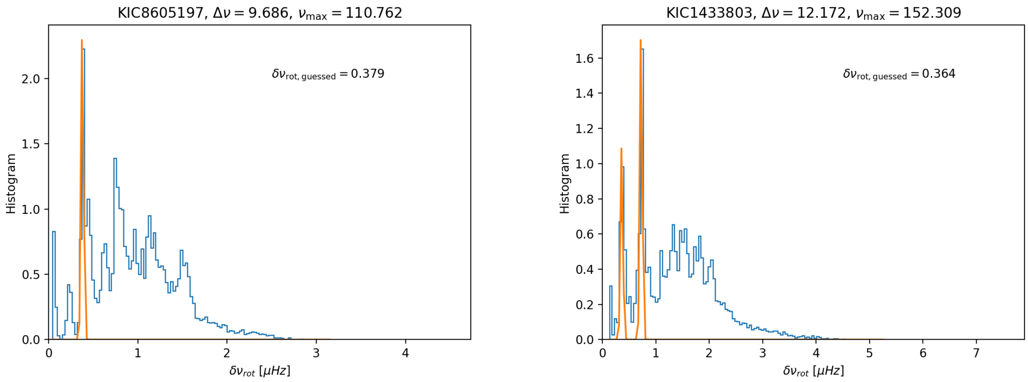

Figure 6.2.: The histogram of KIC 8605197 and KIC 1438803 clearly showing duplet and triplet structure, respectively.

The power density spectra as well as the échelle diagrams from Kallinger (2019) assist to make an initial guess whether the star might provide singlets, duplets, or triplets. Some empirical conclusions are found:

- PDS shows rather even distributed modes → peak is unlikely, meaning that the rotational splitting is too high to match the evolutionary phase of the star, and suggests that only the central component is visible.
- PDS shows duplet properties → only one peak is visible, which corresponds to twice the actual rotational split frequency
- PDS shows triplet properties → either two peaks are present, where the one at lower frequency corresponds to the actual rotational splitting, or only one peak is visible that gives the rotational splitting

This behaviour can be observed in Fig. 6.3 where the échelle diagram at the top shows the even distributed single dipole modes, suggesting that this star is seen pole-on. The second and third diagram clearly show duplet and triplet properties, respectively.

Code snippet

A snippet of the *Python3* code is given in Listing 6.1. The term *data_array* is an imported comma-separated value (csv) file including all necessary parameters (see Tab. 5.2).

```
Rotation = np.array([])

```

[1] `https://johannesbuchner.github.io/UltraNest/`

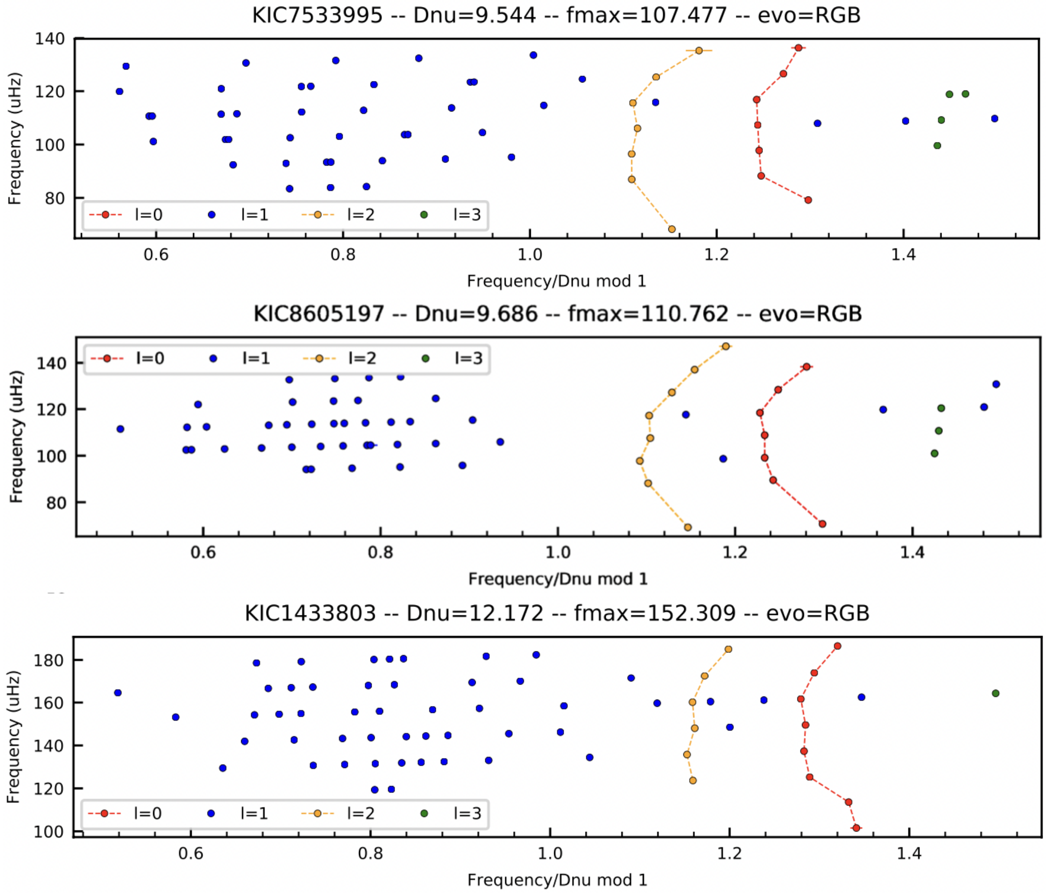

Figure 6.3.: Échelle diagrams of three red giants showing a singlet, a duplet, and a triplet structure in their dipole-mode pattern. Taken from Kallinger (2019).

```python
for m in range(len(data_array)):
    for n in range(5):
        if m+n < len(data_array):
            d_split_guess = data_array.iloc[m+n,1] - data_array.iloc[m,1]
            # data_array.iloc[:,1] = dipole modes
            if d_split_guess < header.iloc[0,1]/6:
            # header.iloc[0,1] = large frequency separation
                for k in range(100):
                    pure = find_nearest(f_mid, data_array.iloc[m,1])
                    rot = rot_split(d_split_guess, header.iloc[0,1],
                          data_array.iloc[m,1], pure)
                    if rot > 0:
                        Rotation = np.append(Rotation, rot)
```

Listing 6.1: Python3 code snippet that scans the dipole-mode spectrum.

6.4. Identifying the real rotational splitting

One major challenge is to disentangle and identify the rotational split-components due to the occurrence of mode crossings. Consecutive rotational multiplets can have overlapping components if the rotation frequency exceeds half the mixed-mode period spacing (Gehan et al., 2017). This can lead to a miss-identification if the split components are identified in ascending order. Stars on the lower giant branch tend to be slow rotators with no crossings. The first crossings occur for moderate rotators at lower frequencies, whereas for rapid rotators many crossings are present (Gehan et al., 2018).
Keeping in mind this phenomenon, a first estimate of the rotational splitting $\delta\nu_{\mathrm{split}}$ based on the initial guess of the g-m mode splitting $\delta\nu_{\mathrm{rot}}$ can be achieved by rearranging Eq. 6.1 into Eq. 6.5.

$$\nu_{\mathrm{n,1,m}} = \nu_{\mathrm{n,1}} + m\mathcal{R}(\nu_{\nu_{\mathrm{n,1,m}}}) \tag{6.5}$$

$\nu_{\mathrm{n,1,m}}$ gives the estimated frequency of the wing components of the multiplet, and further $\delta\nu_{\mathrm{split}}$:

$$\delta\nu_{\mathrm{split}} = \nu_{\mathrm{n,1,m}} - \nu_{\mathrm{n,1}} \tag{6.6}$$

Afterwards, the split-components can be identified straight forward. Starting with the first and lowest dipole mode, it is tested whether there exists a peak in a certain range of $\delta\nu_{\mathrm{split}}$, or $2 \cdot \delta\nu_{\mathrm{split}} \pm 10\%$ for triplets, and duplets, respectively. If there are multiple potential

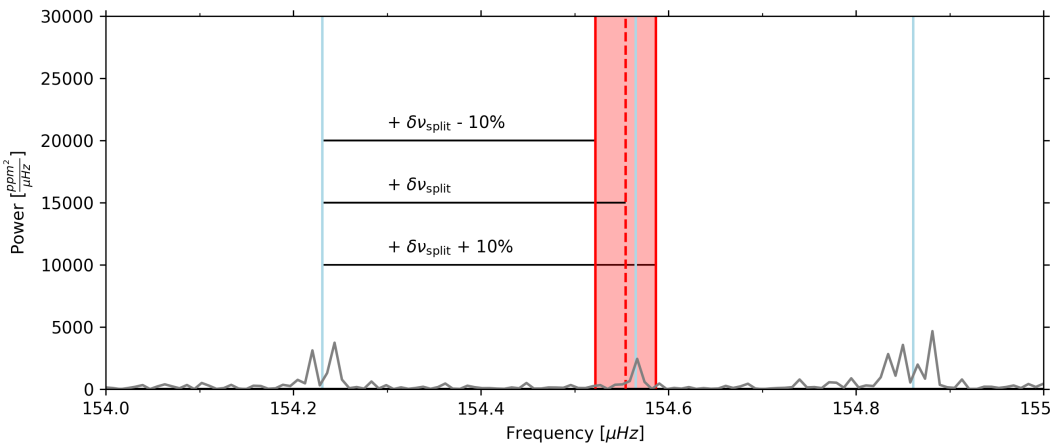

Figure 6.4.: The power spectrum displays a triplet, while the part in red shows the region ($\delta\nu_{\mathrm{split}} \pm 10\%$) in which the potential split-component must lie.

frequencies within this range, the one closest to the middle of the range was selected. The corresponding code snippet (Listing 6.2) shows how triplets are identified. With the detected splittings, the actual, observed rotational splittings $\delta\nu_{\mathrm{split,obs}}$ are calculated and fitted to Eq. 6.7 to get a more accurate estimate of $\delta\nu_{\text{rot}}$.

$$\delta\nu_{\text{split,obs}} = \delta\nu_{\text{rot,guess}} \left(1 - \frac{\lambda}{1 + \left(\frac{\nu - \nu_{\text{p},1}}{\beta \Delta\nu}\right)^2}\right) \tag{6.7}$$

The fits are again performed with UltraNest and two examples are shown in Fig. 6.5.

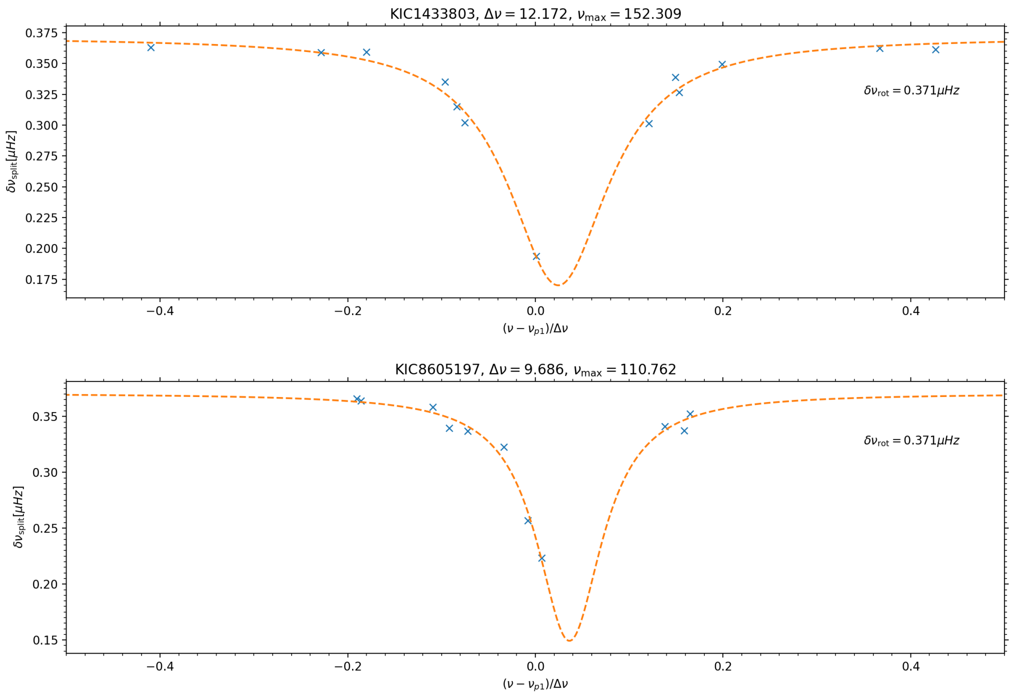

Figure 6.5.: Rotational multiplets of KIC 1433803 (*top*) and KIC 8605197 (*bottom*) fitted with the Lorentzian function in Eq. 6.7 to receive a more accurate value for $\delta\nu_{\text{rot}}$.

Code snippet

The code snippet shows how triplets are identified. It is tested whether a mode is in a range of $\delta\nu_{\mathrm{split}} \pm 10\%$. The mode inside the then used to calculate the range, where the consecutive mode is expected. If this mode is again within the range, a rotational splitting of a dipole mixed mode is fully identified.

```python
modes = np.array([])
true_split = np.array([])

v = 0.1     # deviation of the guessed splitting, in percent
k = 0

while k+2 <= len(df) # dataframe containing nu and guessed split
    v_guess_m = df.iloc[k,0] + df.iloc[k,1] - df.iloc[k,1]*v
    v_guess_p = df.iloc[k,0] + df.iloc[k,1] + df.iloc[k,1]*v

    mod_spl = np.array([])

    for l in range(len(df)):
    """ check whether there exists modes within a certain range """
        if v_guess_m = df.iloc[l,0] <= df.iloc[l,0] <= v_guess_p:
            mod_spl = np.append(mod_spl, df.iloc[l,0])

    if len(mod_spl) != 0:
    """ find the closest mode to the potential split component """
        nearest = find_nearest(mod_split, df.iloc[k,0] + df.iloc[k,1])

        v_nearest_m = nearest + df.iloc[k,1] - df.iloc[k,1]*v
        v_nearest_p = nearest + df.iloc[k,1] + df.iloc[k,1]*v

        mod_spl_1 = np.array([])

        for l in range(len(df)):
            if v_nearest_m <= df.iloc[l,0] <= v_nearest_p:
             mod_spl_1 = np.append(mod_spl_1, df.iloc[l,0])

        if len(mod_spl_1) != 0:
            nearest_fin = find_nearest(mod_spl_1, nearest+df.iloc[k,1])

            """ calculate the real splitting within the triplet """
            tru_spl = abs((df.iloc[k,0] - nearest) + (nearest -
            nearest_fin))/2
            modes = np.append(modes, nearest)
            true_split = np.append(true_split, tru_spl)

            k += 1
        else:
            k += 1
    else:
        k += 1
```

Listing 6.2: Code example of how to identify triplets in a spectrum.

6.5. Estimating the mean core rotation period $\langle T_{\mathrm{rot}} \rangle_c$

In evolved stars like red giants, the inner structure can be considered to consist of two separated regions due to the large density contrast between the core and the envelope. Thus, the observed rotational splitting can be expressed as a sum of two contributions. As dipole g-m mixed mode are mainly sensitive to the core region, the envelope contribution can be neglected, at least for stars on the top of the red giant branch. Including the Ledoux (1951) coefficient for dipole g-m modes, the core rotational splitting is connected to the mean core angular velocity:

$$\delta\nu_{\mathrm{rot,core}} \simeq \frac{1}{2}\left\langle \frac{\Omega}{2\pi} \right\rangle_{\mathrm{core}} \tag{6.8}$$

Although for stars on the lower giant branch, the envelope contribution cannot be neglected and thus a modification has to be implemented to estimate of the mean core rotation rate according to Mosser et al. (2012a):

$$\langle T_{\mathrm{rot}} \rangle_c \equiv \frac{2\pi}{\langle \Omega \rangle_{\mathrm{core}}} \simeq \frac{1}{2\eta\delta\nu_{\mathrm{rot}}} \tag{6.9}$$

where η is a small correction factor, which accounts for the oscillatory propagation in the envelope. According to stellar evolution, at the bottom of the red giant branch, $\delta\nu_{\mathrm{rot}}$ has a larger envelope contribution than at the tip of the red giant branch, where the stellar properties are dominated by the core conditions. Thus, for red giants at different evolutionary stages, this correction factor can be approximated by:

$$\eta \simeq 1 + \gamma \, \frac{\nu_{\mathrm{max}}^2 \Delta\Pi_1}{\Delta\nu} \tag{6.10}$$

where $\gamma \simeq 0.65$, $\Delta\Pi_1$ is the period spacing of gravity modes, and ν_{max} the frequency of maximum oscillation power. Since η is only slightly larger than unity and decreases along the red giant branch due to the increasingly dominating core contribution, this correction factor can also be applied to red clump stars. Furthermore, the contribution of $\Delta\Pi_1$ to η is marginal, suggesting here to use solely an estimate on $\Delta\Pi_1$ making it independent of its complicated determination. According to Fig. 3.1, the gravity mode period spacing is estimated for the different evolutionary stages:

- Red giant branch stars: 90 s
- Red clump stars: 297 s
- 2^{nd} clump stars: 225 s
- Asymptotic giant branch stars (< 1.2 $\mathrm{M}_{\odot}$): 210 s
- Asymptotic giant branch stars (> 1.2 $\mathrm{M}_{\odot}$): 300 s

7. Results and Discussion

Completeness

The mean core rotation rate was successfully measured for 1286 evolved stars, which represents an overall success rate of 50%. The count of stars with their corresponding evolutionary state is shown on the left of Fig. 7.1, whereas the success rate related to the large separation $\Delta\nu$ is shown on the right. In general, this is currently the largest available data

evo	# of stars
RGB	1032
RC	220
2^{nd} RC	31
AGB	3
Σ	1286

$\Delta\nu$	# of stars
$\Delta\nu < 4$	35%
$4 \leq \Delta\nu < 6$	41%
$6 \leq \Delta\nu < 8$	48%
$8 \leq \Delta\nu < 12$	74%
$12 \leq \Delta\nu < 16$	63%
$\Delta\nu \geq 16$	35%

Table 7.1.: Final sample for which at least 3 multiplets were identified.

set of rotational splittings, it exceeds the sample from Gehan et al. (2018) by over 400 stars. Nevertheless, the present method failed to correctly identify the rotational split-components in 1290 stars. Fig. 7.1 shows all unsuccessful (left) and successful (right) cases according to their distinct evolutionary phase. Obviously, the rate of failure increases while $\Delta\nu$ decreases. About 85% (i.e., 1093 stars) of the unsuccessful cases correspond to $\Delta\nu \leq 9.5\mu$Hz. This is not surprising since $\Delta\nu$ decreases towards very low values along the red giant branch, the g-m mode inertia increases, and mixed modes become less visible, which challenges the identification of the rotational components (e.g. Dupret et al. (2009)). Moreover, less evolved stars correspond to higher $\Delta\nu$, hence present only few dipole g-m modes and were probably excluded a priori, or coult not be identified.
Finally, a limited sample of secondary clump and asymptotic giant branch stars were identified, providing at least a hint on the mean core rotation period.

Beyond confusion limit

Gravity-dominated mixed modes are almost equally spaced in period, with a period spacing close to $\Delta\Pi_1$. Thus, for rapid rotators the rotational spitting is expected to exceed the local frequency difference that results from $\Delta\Pi_1$, which causes rotational components of distinct multiplets to overlap. This can result in a misinterpretation of the splittings components. The present method is stable even beyond this confusion limit.

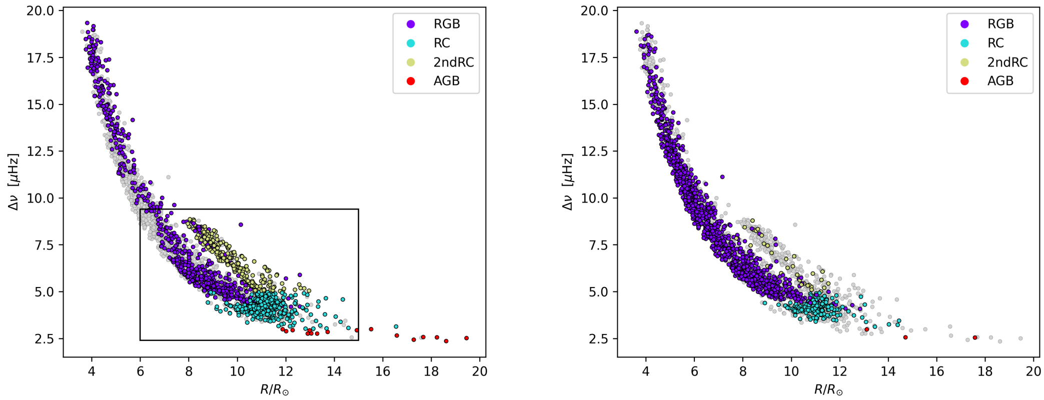

Figure 7.1.: Large separation as a function of radius for evolved stars. The colour-coding distinguished between the various evolutionary stages. *Left*: Unsuccessful stars where the method failed to identify the splitting components. The rectangle shows the region of largest failure of about 85% for $\Delta\nu \leq 9.5$ μHz. *Right*: Successful stars for comparison.

As an example, the overlapping split components for four multiplets of KIC 1996078 are illustrated in Fig. 7.2.

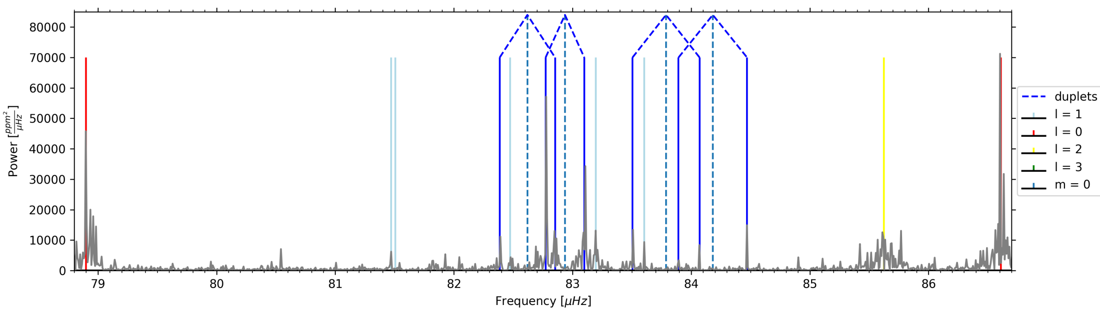

Figure 7.2.: Power density spectrum of KIC 1996078 showing the identification of overlapping split components.

Rotation profiles, λ, and β

The rotation profiles with their corresponding value for λ and β are displayed in Fig. 7.3. λ and β are empirically determined as free parameter, depending on $\Delta\nu$ during the final fit with Eq. 6.7. The function of each fit (in magenta) is shown on the top left side, whereas directly below follows the variation coefficient, giving the scatter in relation to the average of λ and β, respectively.

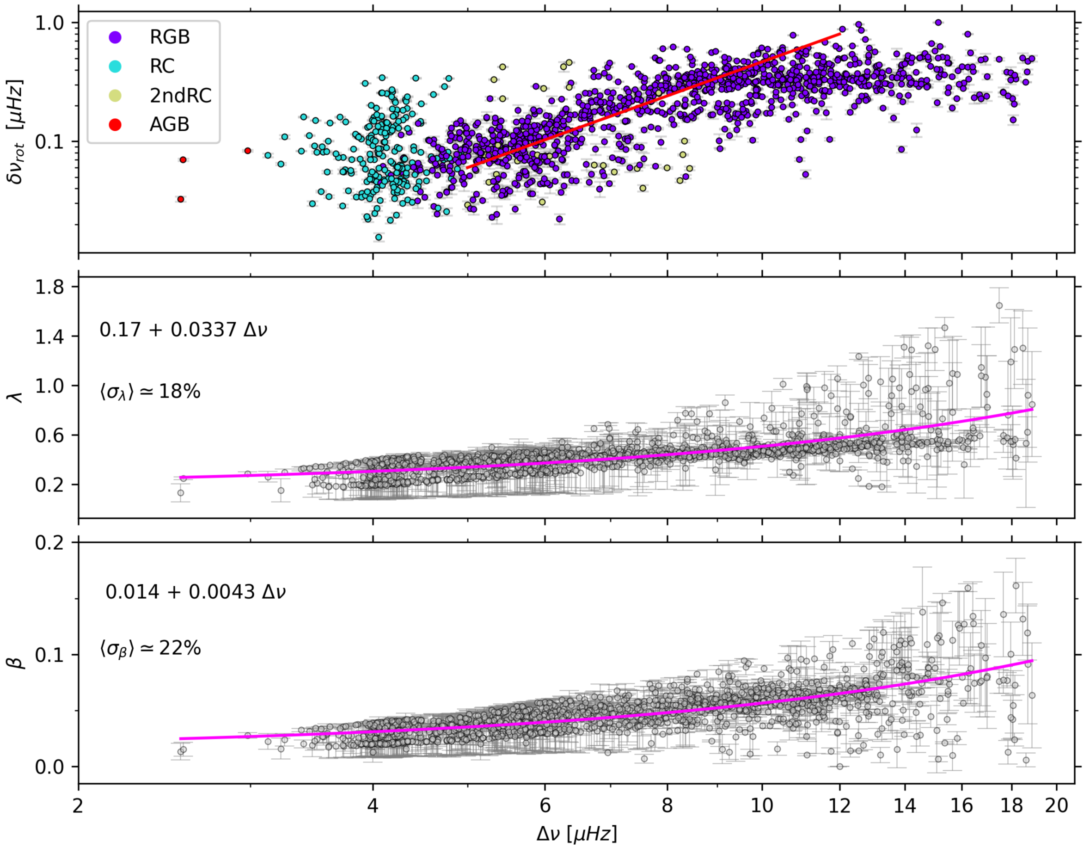

Figure 7.3.: Measured rotational splittings with their corresponding values for λ and β. The red line shows the confusion limit, i.e., approximately the border, above which crossings can occur.

7.1. Comparison with other measurements

The results from this work are compared to the ones obtained by Gehan et al. (2018) who investigated the mean core rotation rate for 875 red giant branch stars by using stretched spectra. As illustrated in Fig. 7.4, the mean core rotation rate for 371 common stars is plotted against each other, including the 1:1, 2:1 and 1:2 relation. The relative difference between the present measurements and those of Gehan et al. (2018) are calculated as:

$$d_r = \left| \frac{\delta\nu_{\mathrm{rot}} - \delta\nu_{\mathrm{rot},2018}}{\delta\nu_{\mathrm{rot},2018}} \right| \tag{7.1}$$

I found that $d_r < 10\%$ for 268 stars (~ 72 %), $10\% < d_r < 15\%$ for 35 stars, while the rest is mainly distributed nigh the 2:1 relation. One must keep in mind that the method used in the present work is a simplified approach, leading to a highly satisfying compatibility with other measurements. This work is independent of any challenging estimation of $\Delta\Pi_1$ but relies on a Lorentzian profile to reproduce the observed modulation of rotational splittings, which was only found to fit best and has no theoretical basis. Additionally,

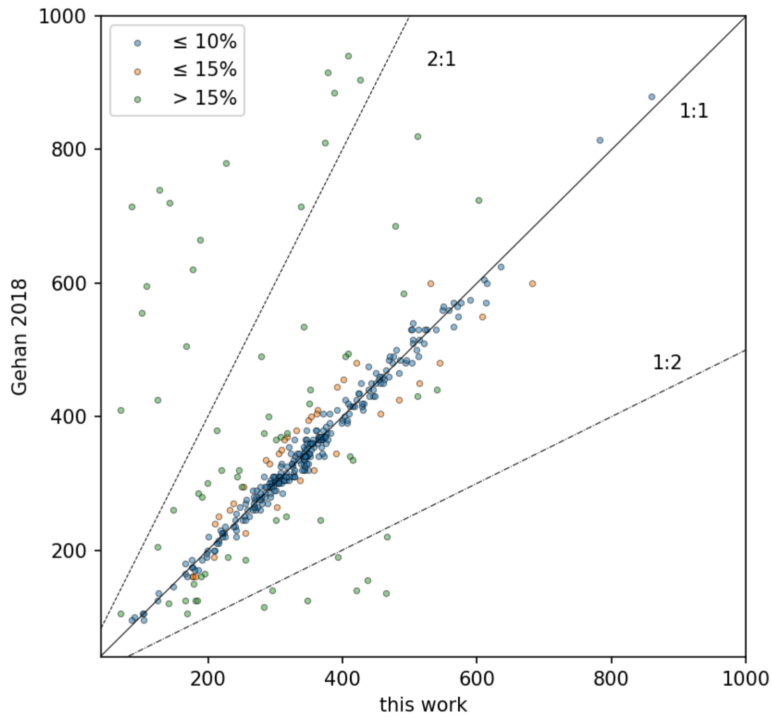

Figure 7.4.: Comparison of rotational splittings (in nHz) from Gehan et al. (2018) with the ones from this work. The comparable sample contains a total number of 371 stars, where 268 show a relative difference below 10% (blue), 35 stars between 10% and 15% (orange) while the remaining 68 stars (green) are mainly distributed nigh the 2:1 relation.

I compared the present sample with the common stars from Mosser et al. (2012a) who used as well a Lorentzian approach. Thus, it was rather surprising that the compatibility is below 50%. Mosser et al. (2012a) found rotational splittings at very low frequencies, where the present method clearly suggested a higher rotational splitting. Note here that Mosser et al. (2012a) measured a maximum splitting of around 600 nHz, Gehan et al. (2018) around 900 nHz while this work indicates values up to approximately 1 μHz.

7.2. Evolution of the core rotation

For the evolution of the core rotation throughout the various evolutionary stages, radius, mass, and effective temperature are used from APOKASC (Pinsonneault et al., 2018), if available. Otherwise, it is estimated through scaling relations from Sec. 2.4.1 and Eq. 7.2:

$$T_{\mathrm{eff}} = 4800 \left(\frac{\nu_{\mathrm{max}}}{40} \right)^{0.06} \tag{7.2}$$

On the red giant branch

The mean core rotation rate calculated as described in Sec. 6.5 is shown in Fig. 7.5 for red giant branch stars. The present results suggest a clear increase of the mean core

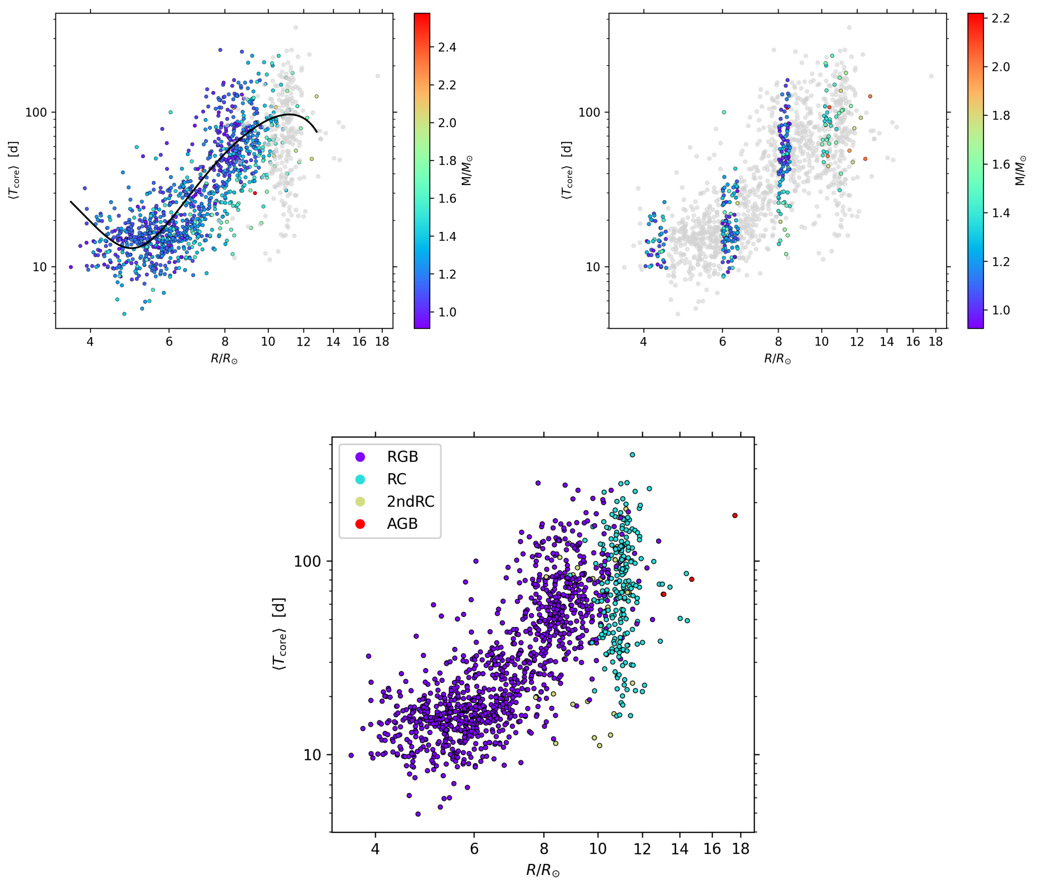

Figure 7.5.: Mean core rotation period as a function of stellar radius on a log-log scale. *Top*: The coloured dots show red-giant branch stars with different masses. The grey dots resemble the total evaluated sample. *Bottom*: Total sample, with colour-coding showing the evolutionary phase.

rotation period as the star climbs the red giant branch. During red-giant evolution, the core contracts while the envelope expands, thus leading to a general increase in radius. Conservation of angular momentum $J = I \cdot \omega$ with I being the moment of inertia ($= M \cdot R^2$) and ω the angular speed [in $kg \cdot m^2 \cdot s^{-1}$] supports this result (Aerts et al., 2019). As the core contracts, its radius decreases, leading to an accelerated angular speed to maintain angular momentum. Thus, solely derived from an observational point of view, the core shows a steep braking from the bottom to the tip of the red giant branch.
On the lower red giant branch, the low core rotation periods are in agreement with what was found by Gehan et al. (2018) and Mosser et al. (2012a). Although the steep increase is in contrast to what was found by Gehan et al. (2018) suggesting rather constant core rotation during the red giant branch evolution. Similarities were found by comparing with the results from Mosser et al. (2012a) suggesting a significant slow-down during red-giant branch evolution.
Furthermore, Fig. 7.5 (*top left*) suggests a slight mass dependence so that higher mass stars tentatively show a lower core ration period compared to less massive stars at comparable radius (*top right*). The four stripes show distinct ranges of stellar radius: 4 $\leq R/R_\odot \leq$ 4.5, 6 $\leq R/R_\odot \leq$ 6.5, 8 $\leq R/R_\odot \leq$ 8.5 and $R/R_\odot \geq$ 10. A mass dependence can only be guessed at 8 - 8.5 $R/R_\odot$.

In general

The mean core rotation rate for the total sample including all evolutionary phases, as well as all stars from Tab. 4.1, can be seen in Fig. 7.6. Star symbols mark the stars from the present study, whereas the dots with different colours are from Deheuvels et al., from distinct years. During the main-sequence, stars are believed to rotate nearly uniformly. After the core hydrogen gets gradually exhausted, the star leaves the main-sequence and enters the subgiant stadium. The core starts to contract and spin up. The youngest subgiants in the sample show nearly solid-body rotation, while the other slightly more evolved subgiants and young red giants already show a steep acceleration of the core rotation. Unfortunately, the transition region towards the bottom of the red giant branch is lacking data. At least a few stars would be helpful to estimate the transition.
Red clump stars cover a vertical, narrow stripe roughly between 10 and 12 $R_\odot$ with mass increasing with radius. The constraint region is caused by the unstable manner of helium ignition during stellar evolution. This contrasts with secondary clump stars, which undergo a gradual helium ignition and are thus wider spread. Compared to the previous red giant phase, the stellar radius is decreased. Meaning that the envelope contracted while the core expanded. The rotation in the central regions of the star further slowed down. Note here that due to the convective core in red clump and secondary clump stars, the core rotation rates are constraint by the near core regions. Finally, in this work also three asymptotic giant branch stars could be measured and settle to bottom right region showing a slow rotation rate.

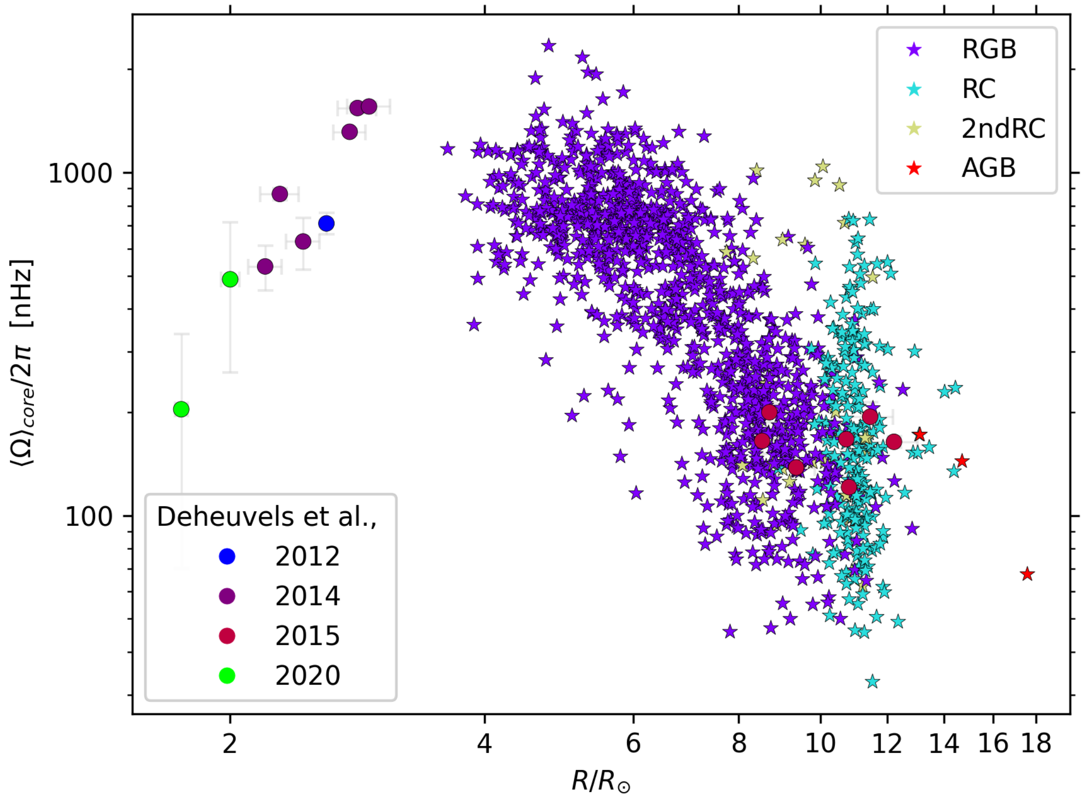

Figure 7.6.: Mean core rotation rate during stellar evolution for various samples represented as dots; two young subgiants in green (Deheuvels et al., 2020), five subgiants and an early red giant in purple (Deheuvels et al., 2014), another early red giant in blue from (Deheuvels et al., 2012), and seven secondary clump stars in red (Deheuvels et al., 2015). The star symbols show the data of this work at distinct evolutionary phases.

From an observational point of view, in Fig. 7.6, it seems like the acceleration track of the core during the subgiant evolution is orthogonal to the core rotation braking track towards the tip of the red giant branch. This would mean that both tracks would follow the same exponential function, but with a different sign. In Fig. 7.7 this idea was tested by fitting an exponential function to the low-mass subgiants and early red giant from Fig. 7.6, and to solely red giants. It was found that the gradient of the mean core rotation rate during the subgiant evolution is in absolute value roughly 2.3 times higher than on the red giant branch.

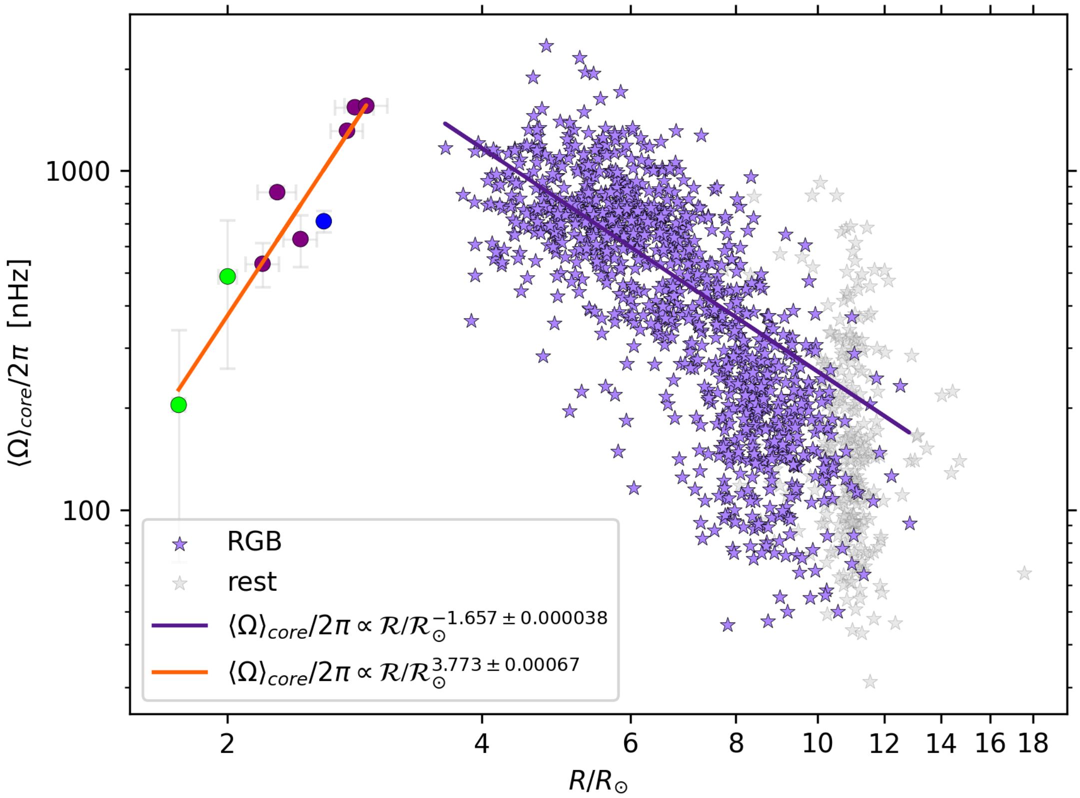

Figure 7.7.: Mean core rotation rate during stellar evolution for various samples represented as dots; two young subgiants in green (Deheuvels et al., 2020), five subgiants and an early red giant in purple (Deheuvels et al., 2014), another early red giant in blue from (Deheuvels et al., 2012). The star symbols show the data of this work for red giants, while the grey star symbols show the full data extent.

Low-mass stars with 1 $M_\odot$ have a long-lived subgiant branch phase ($\sim$ 2 Gyr), while an intermediate mass star with 5 $M_\odot$ spends *"only"* approximately 2 million years (Pols, 2011) on it. Thus, it would be interesting if the same effect that accelerates the stellar core on the subgiant branch works on both timescales. The same, but decelerating, expectations are found on the red giant branch, since a 1 $M_\odot$ spends roughly $5 \cdot 10^8$ yrs, while for a 5 $M_\odot$ it takes only a few 10^7 yrs before helium is ignited in the core (Pols, 2011). Furthermore, it would be of great interest to investigate this diagram for more massive stars than in the current sample.

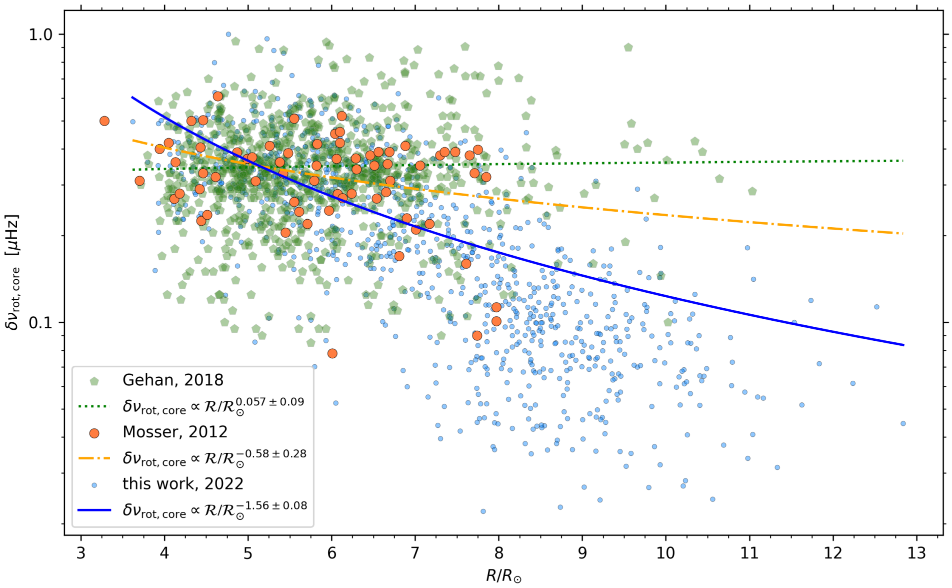

Figure 7.8.: Comparison of the measured slow-down rates as a function of the stellar radius from red giant branch stars in Mosser et al. (2012a) (orange dots), Gehan et al. (2018) (green pentagons) and the measurements obtained in this study (blue dots).

7.3. Slow-down along the red giant branch

The slow-down rate as function of stellar radius for red giant branch stars from Mosser et al. (2012a) and Gehan et al. (2018) in comparison with the measurements obtained in this study is illustrated in Fig. 7.8. The small light-blue dots show the mean core rotational splitting from this work, the large orange dots represent the ones from Mosser et al. (2012a), and the green pentagons the results obtained by Gehan et al. (2018). Following the approach Gehan et al. (2018): $\delta\nu_{\mathrm{rot}} \propto (R/R_{\odot})^{a}$ with the values for a fitted with *Ultranest* as a free parameter (see Fig. 7.2). The slopes indicate that the slow-down rate is strongest for the results obtained in this work with $\delta\nu_{\mathrm{rot}} \propto (R/R_{\odot})^{-1.56\pm0.08}$. Which seem obvious considering the lower core rotation rates of clump and asymptotic giant branch stars (see Fig. 7.6). Thus, there must occur a steep but continuous braking along the red giant branch rather than an abrupt one. This is followed by the gradual decline from Mosser et al. (2012a), $\delta\nu_{\mathrm{rot}} \propto (R/R_{\odot})^{-0.58\pm0.28}$. While for Gehan et al. (2018) the core rotate is continuous throughout the red giant branch, $\delta\nu_{\mathrm{rot}} \propto (R/R_{\odot})^{0.057\pm0.08}$.

The slow-down rates as a function of stellar mass for red giant branch stars is illustrated in Fig. 7.9 with the corresponding values in Tab. 7.3.

a_{2012}	a_{2018}	a_{2022}
-0.58 ± 0.28	0.057 ± 0.09	-1.56 ± 0.08

Table 7.2.: Measured slow-down rates as a function of the stellar radius from red giant branch stars in Mosser et al. (2012a), Gehan et al. (2018) and the measurements obtained in this study.

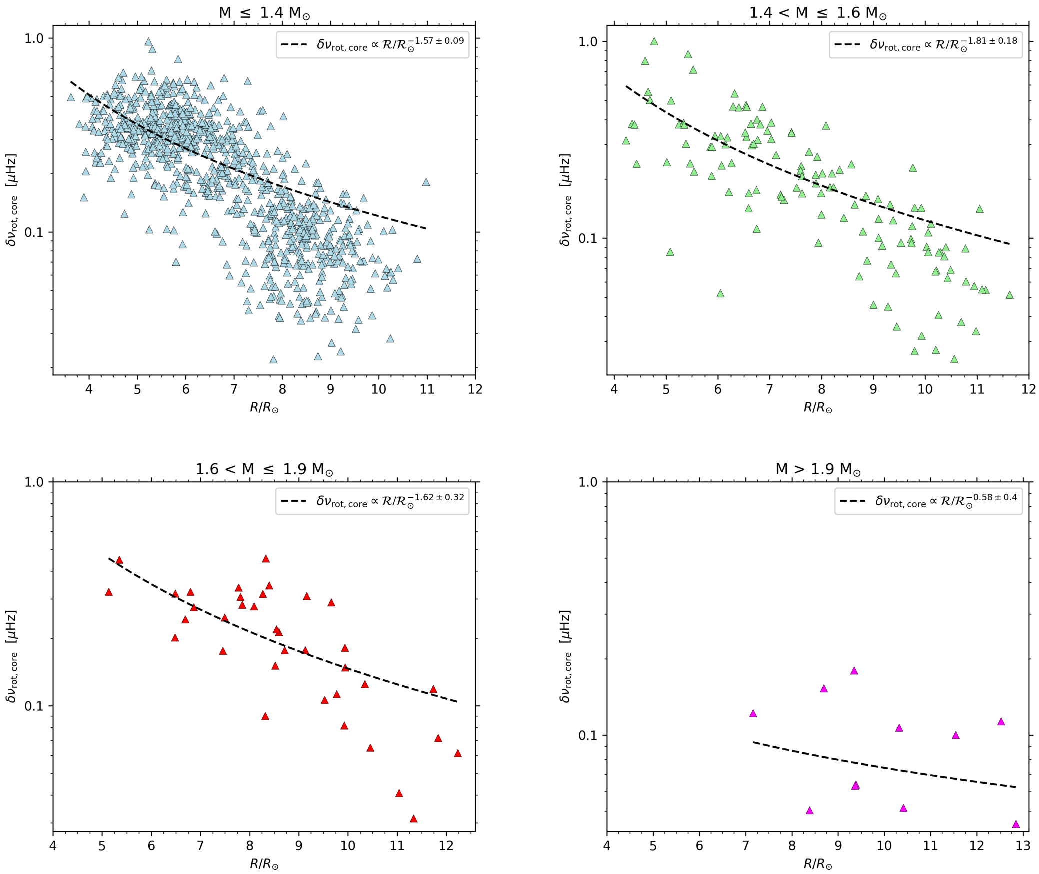

Figure 7.9.: Comparison of the measured slow-down rates as a function of the stellar radius of red giants. The mass ranges are written on the top of each figure.

mass range	a_{2022}	$\langle \delta\nu_{\mathrm{rot},2022} \rangle$
$M \leq 1.4 M_{\odot}$	-1.57 ± 0.09	221 ± 152
$1.4 < M \leq 1.6 M_{\odot}$	-1.81 ± 0.18	203 ± 168
$1.6 < M \leq 1.9 M_{\odot}$	-1.62 ± 0.32	182 ± 117
$M > 1.9 M_{\odot}$	-0.58 ± 0.4	107 ± 106

Table 7.3.: Measured slow-down rates and mean rotational splittings as a function of stellar radius for different mass ranges in the present study.

8. Conclusion

Stellar evolution codes show astonishing accuracy, but when it comes to rotation and angular momentum transport, they overestimate the core rotation rates during the post-main-sequence evolution. In practice, stellar rotation models can satisfyingly reproduce the surface rotation rates, as well as the global seismic parameters, i.e., $\Delta\nu$ and $\nu_{\rm max}$, but they fail to reproduce the rapid core rotation rates from observations along the post-main-sequence phase. Thus, there must be an efficient mechanism at work that transport angular momentum in the stellar interior during a stars' evolution besides the usual hydrodynamical processes.

Dipole mixed modes provide the ability to examine the core rotation rates, whereas the rotational splitting of each mode, based on the inclination of the star, defines whether there are singlets ($i \approx 0°$), duplets ($i \approx 90°$), or triplets (i in-between), expected in the power density spectra. The frequency separation between the respective splitting components is a measure of the core rotation rate if the envelope contribution can be neglected. The correct disentangling of the rotational splitting components is crucial because mode crossings can occur, when the rotational splitting exceeds half the mixed-mode spacing. An automated, simple but precise approach has been performed, which is further independent of $\Delta\Pi_1$ and even works beyond the confusion limit. At first, the maximum rotational splitting of gravity-dominated mixed modes $\delta\nu_{\rm rot,guess}$ is estimated via a histogram showing the most common width ($\delta\nu_{\rm split,guess}$) between dipole mixed modes. Depending on the count of unambiguous peaks in the histogram, either singlets, duplets, or triplets are expected. If singlets are detected, no rotational splitting can be extracted, while duplets contain twice the $\delta\nu_{\rm rot,guess}$, and triplets once the $\delta\nu_{\rm rot,guess}$. With $\delta\nu_{\rm rot,guess}$, $\delta\nu_{\rm split}$ is calculated, and can afterwards be fitted with a Lorentzian function to get a more accurate $\delta\nu_{\rm rot}$.

The full sample extends over 6179 red giants, where roughly a third displayed a promising histogram. Although the mean core rotation rates were extracted for only 1286 stars, it represents a success rate of approximately 50%. The stars are distributed across the red giant branch up to the asymptotic giant branch. Nevertheless, this sample is currently the largest one and further includes three stars on the asymptotic giant branch. In comparison with $\delta\nu_{\rm rot}$ of Gehan et al. (2018), using stretched spectra, a satisfactory agreement was found. Roughly 72% of cases have a relative difference below 10%. Although a similar approach like in Mosser et al. (2012a) was used, only approximately 50% of cases share a comparable $\delta\nu_{\rm rot}$. Mosser et al. (2012a) was able to identify rotational splittings at very low frequencies, where the present method clearly suggested a higher rotational splitting.

After hydrogen is exhausted in the core and the star has reached the end of the main-sequence, the star experiences structural changes that drive differential rotation. Under the assumption of conservation of angular momentum, during the stellar evolution towards the red giant branch, the contraction of the central layers of the star spins up the core, while the envelope expands and spins down. A steep gradient develops. Stars reach their maximum mean core rotation rate at the transition region from the subgiant branch to the base of the red giant branch, where the core is slowed down afterwards. During the ascend on the red giant branch, angular momentum must be redistributed from the core into the envelope, braking the core, while accelerating the envelope. Furthermore, the incline of the core rotation rate along the subgiant evolution ($(R/R_{\odot})^{3.773}$) is in absolute value approximately 2.3 times higher than the decline on the red giant branch ($(R/R_{\odot})^{-1.657}$). The mechanism responsible for this observational finding is still unknown. Therefore, this study extends the available data and provides the opportunity of further investigation on the redistribution of angular momentum at different evolutionary phases.

A hint on mass dependence, suggesting that higher mass stars tend to have a lower core rotation period compared to less massive stars at a comparable radius, can only be guessed at 8-8.5 $R/R_{\odot}$. Thus, no direct relation had been found.

While Gehan et al. (2018) suggests that the core rotation rates remains rather constant along the red giant branch, Mosser et al. (2012a) suggests a gradual decline. The results in this work support the findings of Mosser et al. (2012a), although its decline (a) of $\delta\nu_{\mathrm{rot}} \propto (R/R_{\odot})^{a}$ is roughly three times higher (see Tab. 7.2). Therefore, the slow-down of the core rotation is more efficient than expected.

Future research could build on these results and test possible mechanisms that are potentially responsible for angular momentum transport in stellar interiors, e.g., additional viscosity, Tayler-Spruit dynamos, and so forth. With this work, I hope to contribute to the overall understanding of the stellar interior, and the improvement of current stellar evolution models.

Bibliography

Aerts, C. (2021). Probing the interior physics of stars through asteroseismology. *Reviews of Modern Physics*, 93(1):015001.

Aerts, C., Christensen-Dalsgaard, J., and Kurtz, D. W. (2010). *Asteroseismology*.

Aerts, C., Mathis, S., and Rogers, T. M. (2019). Angular Momentum Transport in Stellar Interiors. , 57:35–78.

Beck, P. G. and Kallinger, T. (2013). Das Echo aus der Tiefe. *Sterne und Weltraum*, 52(4):50–58.

Beck, P. G., Montalban, J., Kallinger, T., De Ridder, J., Aerts, C., García, R. A., Hekker, S., , M.-A., Mosser, B., Eggenberger, P., Stello, D., Elsworth, Y., Frandsen, S., Carrier, F., Hillen, M., Gruberbauer, M., Christensen-Dalsgaard, J., Miglio, A., Valentini, M., Bedding, T. R., Kjeldsen, H., Girouard, F. R., Hall, J. R., and Ibrahim, K. A. (2012). Fast core rotation in red-giant stars as revealed by gravity-dominated mixed modes. , 481(7379):55–57.

Bedding, T. R. and Kjeldsen, H. (2003). Solar-like Oscillations. , 20(2):203–212.

Brown, T. M., Gilliland, R. L., Noyes, R. W., and Ramsey, L. W. (1991). Detection of Possible p-Mode Oscillations on Procyon. , 368:599.

Buchner, J. (2016). A statistical test for Nested Sampling algorithms. *Statistics and Computing*, 26(1-2):383–392.

Buchner, J. (2019). Collaborative Nested Sampling: Big Data versus Complex Physical Models. , 131(1004):108005.

Buchner, J. (2021). UltraNest - a robust, general purpose Bayesian inference engine. *The Journal of Open Source Software*, 6(60):3001.

Christensen-Dalsgaard, J. (1984). What Will Asteroseismology Teach us. In Mangeney, A. and Praderie, F., editors, *Space Research in Stellar Activity and Variability*, page 11.

Cowling, T. G. (1941). The non-radial oscillations of polytropic stars. , 101:367.

De Ridder, J., Barban, C., Baudin, F., Carrier, F., Hatzes, A. P., Hekker, S., Kallinger, T., Weiss, W. W., Baglin, A., Auvergne, M., Samadi, R., Barge, P., and Deleuil, M. (2009). Non-radial oscillation modes with long lifetimes in giant stars. , 459(7245):398–400.

Deheuvels, S., Ballot, J., Beck, P. G., Mosser, B., Østensen, R., García, R. A., and Goupil, M. J. (2015). Seismic evidence for a weak radial differential rotation in intermediate-mass core helium burning stars. , 580:A96.

Deheuvels, S., Ballot, J., Eggenberger, P., Spada, F., Noll, A., and den Hartogh, J. W. (2020). Seismic evidence for near solid-body rotation in two kepler subgiants and implications for angular momentum transport. *Astronomy Astrophysics*, 641:A117.

Deheuvels, S., Doğan, G., Goupil, M. J., Appourchaux, T., Benomar, O., Bruntt, H., Campante, T. L., Casagrande, L., Ceillier, T., Davies, G. R., De Cat, P., Fu, J. N., García, R. A., Lobel, A., Mosser, B., Reese, D. R., Regulo, C., Schou, J., Stahn, T., Thygesen, A. O., Yang, X. H., Chaplin, W. J., Christensen-Dalsgaard, J., Eggenberger, P., Gizon, L., Mathis, S., Molenda-Żakowicz, J., and Pinsonneault, M. (2014). Seismic constraints on the radial dependence of the internal rotation profiles of six Kepler subgiants and young red giants. , 564:A27.

Deheuvels, S., García, R. A., Chaplin, W. J., Basu, S., Antia, H. M., Appourchaux, T., Benomar, O., Davies, G. R., Elsworth, Y., Gizon, L., Goupil, M. J., Reese, D. R., Regulo, C., Schou, J., Stahn, T., Casagrande, L., Christensen-Dalsgaard, J., Fischer, D., Hekker, S., Kjeldsen, H., Mathur, S., Mosser, B., Pinsonneault, M., Valenti, J., Christiansen, J. L., Kinemuchi, K., and Mullally, F. (2012). Seismic Evidence for a Rapidly Rotating Core in a Lower-giant-branch Star Observed with Kepler. , 756(1):19.

Dupret, M. A., Belkacem, K., Samadi, R., Montalban, J., Moreira, O., Miglio, A., Godart, M., Ventura, P., Ludwig, H. G., Grigahcène, A., Goupil, M. J., Noels, A., and Caffau, E. (2009). Theoretical amplitudes and lifetimes of non-radial solar-like oscillations in red giants. , 506(1):57–67.

Eyer, L. and Bartholdi, P. (1999). Variable stars: Which Nyquist frequency? , 135:1–3.

Eyer, L. and Mowlavi, N. (2008). Variable stars across the observational HR diagram. In *Journal of Physics Conference Series*, volume 118 of *Journal of Physics Conference Series*, page 012010.

Gehan, C., Mosser, B., and Michel, E. (2017). Rapidly rotating red giants. In *European Physical Journal Web of Conferences*, volume 160 of *European Physical Journal Web of Conferences*, page 04005.

Gehan, C., Mosser, B., Michel, E., Samadi, R., and Kallinger, T. (2018). Core rotation braking on the red giant branch for various mass ranges. , 616:A24.

Gough, D. O. (1986). Solar and solar-like oscillations: theory. *Highlights of Astronomy*, 7:283–293.

Hekker, S. and Christensen-Dalsgaard, J. (2017). Giant star seismology. , 25(1):1.

Houdek, G., Balmforth, N. J., Christensen-Dalsgaard, J., and Gough, D. O. (1999). Amplitudes of stochastically excited oscillations in main-sequence stars. , 351:582–596.

Howell, S. B. (2020). *The NASA Kepler Mission.*

Huber, D., Bedding, T. R., Stello, D., Mosser, B., Mathur, S., Kallinger, T., Hekker, S., Elsworth, Y. P., Buzasi, D. L., De Ridder, J., Gilliland, R. L., Kjeldsen, H., Chaplin, W. J., García, R. A., Hale, S. J., Preston, H. L., White, T. R., Borucki, W. J., Christensen-Dalsgaard, J., Clarke, B. D., Jenkins, J. M., and Koch, D. (2010). Asteroseismology of Red Giants from the First Four Months of Kepler Data: Global Oscillation Parameters for 800 Stars. , 723(2):1607–1617.

Huber, D. and Zwintz, K. (2020). Solar-Like Oscillations: Lessons Learned & First Results from TESS. In Neiner, C., Weiss, W. W., Baade, D., Griffin, R. E., Lovekin, C. C., and Moffat, A. F. J., editors, *Stars and their Variability Observed from Space*, pages 457–463.

Kallinger, T. (2019). Release note: Massive peak bagging of red giants in the kepler field.

Kallinger, T., Beck, P. G., Stello, D., and Garcia, R. A. (2018). Non-linear seismic scaling relations. *Astronomy &amp Astrophysics*, 616:A104.

Kallinger, T., Guenther, D. B., Weiss, W. W., Hareter, M., Matthews, J. M., Kuschnig, R., Reegen, P., Walker, G. A. H., Rucinski, S. M., Moffat, A. F. J., and Sasselov, D. (2008). MOST found evidence for solar-type oscillations in the K2 giant star HD 20884. *Communications in Asteroseismology*, 153:84–103.

Kallinger, T., Hekker, S., Mosser, B., De Ridder, J., Bedding, T. R., Elsworth, Y. P., Gruberbauer, M., Guenther, D. B., Stello, D., Basu, S., García, R. A., Chaplin, W. J., Mullally, F., Still, M., and Thompson, S. E. (2012). Evolutionary influences on the structure of red-giant acoustic oscillation spectra from 600d of Kepler observations. , 541:A51.

Kippenhahn, R., Weigert, A., and Weiss, A. (2012). *Stellar Structure and Evolution.*

Kjeldsen, H. and Bedding, T. R. (1995). Amplitudes of stellar oscillations: the implications for asteroseismology. , 293:87–106.

Kurtz, D. (2022). Asteroseismology across the HR diagram. In *Annual Conference and General Assembly of the African Astronomical Society*, page 1.

Lamb, H. (1932). *Hydrodynamics.*

Lamers, H. J. G. L. M. and Levesque, E. M. (2017). *Understanding Stellar Evolution.*

Ledoux, P. (1951). The Nonradial Oscillations of Gaseous Stars and the Problem of Beta Canis Majoris. , 114:373.

Leighton, R. B., Noyes, R. W., and Simon, G. W. (1962). Velocity Fields in the Solar Atmosphere. I. Preliminary Report. , 135:474.

Maeder, A. (2009). *Physics, Formation and Evolution of Rotating Stars.*

Mosser, B. (2015). Stellar oscillations - i - the adiabatic case. *EAS Publications Series*, 73-74:3–110.

Mosser, B., Benomar, O., Belkacem, K., Goupil, M. J., Lagarde, N., Michel, E., Lebreton, Y., Stello, D., Vrard, M., Barban, C., Bedding, T. R., Deheuvels, S., Chaplin, W. J., De Ridder, J., Elsworth, Y., Montalban, J., Noels, A., Ouazzani, R. M., Samadi, R., White, T. R., and Kjeldsen, H. (2014). Mixed modes in red giants: a window on stellar evolution. , 572:L5.

Mosser, B., Goupil, M. J., Belkacem, K., Marques, J. P., Beck, P. G., Bloemen, S., De Ridder, J., Barban, C., Deheuvels, S., Elsworth, Y., Hekker, S., Kallinger, T., Ouazzani, R. M., Pinsonneault, M., Samadi, R., Stello, D., García, R. A., Klaus, T. C., Li, J., Mathur, S., and Morris, R. L. (2012a). Spin down of the core rotation in red giants. , 548:A10.

Mosser, B., Goupil, M. J., Belkacem, K., Michel, E., Stello, D., Marques, J. P., Elsworth, Y., Barban, C., Beck, P. G., Bedding, T. R., De Ridder, J., García, R. A., Hekker, S., Kallinger, T., Samadi, R., Stumpe, M. C., Barclay, T., and Burke, C. J. (2012b). Probing the core structure and evolution of red giants using gravity-dominated mixed modes observed with Kepler. , 540:A143.

Pinsonneault, M. H., Elsworth, Y. P., Tayar, J., Serenelli, A., Stello, D., Zinn, J., Mathur, S., García, R. A., Johnson, J. A., Hekker, S., Huber, D., Kallinger, T., Mészáros, S., Mosser, B., Stassun, K., Girardi, L., Rodrigues, T. S., Silva Aguirre, V., An, D., Basu, S., Chaplin, W. J., Corsaro, E., Cunha, K., García-Hernández, D. A., Holtzman, J., Jönsson, H., Shetrone, M., Smith, V. V., Sobeck, J. S., Stringfellow, G. S., Zamora, O., Beers, T. C., Fernández-Trincado, J. G., Frinchaboy, P. M., Hearty, F. R., and Nitschelm, C. (2018). The Second APOKASC Catalog: The Empirical Approach. , 239(2):32.

Pols, O. (2011). *Stellar Structure and Evolution*. Astronomical Institute Utrecht.

Schönberg, M. and Chandrasekhar, S. (1942). On the Evolution of the Main-Sequence Stars. , 96:161.

Scuflaire, R. (1974). The Non Radial Oscillations of Condensed Polytropes. , 36:107.

Tassoul, M. (1980). Asymptotic approximations for stellar nonradial pulsations. , 43:469–490.

Ulrich, R. K. (1986). Determination of Stellar Ages from Asteroseismology. , 306:L37.

White, T. R., Bedding, T. R., Stello, D., Appourchaux, T., Ballot, J., Benomar, O., Bonanno, A., Broomhall, A.-M., Campante, T. L., Chaplin, W. J., Christensen-Dalsgaard, J., Corsaro, E., Doğan, G., Elsworth, Y. P., Fletcher, S. T., García, R. A., Gaulme, P., Handberg, R., Hekker, S., Huber, D., Karoff, C., Kjeldsen, H., Mathur, S., Mosser, B., Monteiro, M. J. P. F. G., Régulo, C., Salabert, D., Silva Aguirre, V., Thompson, M. J., Verner, G., Morris, R. L., Sanderfer, D. T., and Seader, S. E. (2011). Asteroseismic Diagrams from a Survey of Solar-like Oscillations with Kepler. , 742(1):L3.

A. Appendix

The code is written in Python3 and is given in full extent below. Basically, I worked with comma-separated values (csv) files and used UltraNest for fitting.
From row 21 - 75 UltraNest is implemented. The free yet unknown parameters in row 21 and 50 are set for the Gaussian and Lorentzian fit. For both uniform prior parameters must be chosen. The selected Gaussian likelihood function is evaluated at each position x and compared with the model (41, 69). This likelihood defines how far the data points are from the model predictions. The sampler runs at minimum N = 400 live points, and as a result, the posterior parameters are computed (i.e., for each free parameter: mean, standard deviation, median, upper, and lower 1-σ error).
The overall definitions are given from row 76 - 201 see description therein.
Finally, the program can run (204), and follows the flow chart Fig. 6.1. At first, the data for the histogram is calculated (227 - 239) as outlined in Sec. 6.3. The resulting histogram is then fitted with a (double) Gaussian to receive the expected value for $\delta\nu_{\mathrm{rot,guess}}$. At this point one needs to decide, whether the histogram shows an unambiguous singlet, duplet, or triplet structure. If in the histogram a clear structure is visible, $\delta\nu_{\mathrm{rot,guess}}$ can be chosen according to the empirical conclusions from Sec. 6.3. Otherwise, one can either re-run the scanning procedure, or exist, and proceed with the next star. There is no maximum iteration limit set here. One must subjectively decide when to stop and exit the loop.
The next step is to estimate with $\delta\nu_{\mathrm{rot,guess}}$ the frequency of the split-components (276 - 288) as described in more detail in Sec. 6.4. Afterwards, these potential frequencies are tested whether they are located in certain distance of $\delta\nu_{\mathrm{split}}$ $\pm 10\%$ for triplets (289 - 336), or $2 \cdot \delta\nu_{\mathrm{split}}$ $\pm 10\%$ for duplets (346 - 372). If there are various modes within this range, the one closest to the mean is chosen. If the rotational splitting components are successfully identified, a Lorentzian fit is performed to get a more accurate estimate of $\delta\nu_{\mathrm{rot}}$. Are less than three multiplets identified, the process breaks directly and proceeds with the next star.

```
1 import csv
2 import glob
3 import sys
4 from time import perf_counter
5 from pathlib import Path
6 import configparser
7 import numpy as np
8 import pandas as pd
9 import matplotlib.pyplot as plt
10 import ultranest
11 from wand.image import Image as WImage
12 from wand.display import display
```

```
import matplotlib.ticker as ticker
from matplotlib.ticker import MultipleLocator

config = configparser.ConfigParser()
config.read('config.ini')

#---------- UltraNest Parameters for Gaussian fit ----------

parameters = ['amp1','amp2', 'mu1']

def prior_transform(cube):

    params = cube.copy()

    for i in range(len(params)):
        params[i] = cube[i]* (hi[i]-lo[i]) + lo[i]

    return params

def my_likelihood(params):

    amp1, amp2, mu1 = params
    y_model = gaussian(x, amp1, amp2, mu1)

    like = -0.5 * (((y_model - y) / yerr)**2).sum()

    return like

def gaussian(x, amp1, amp2, mu1):

    s = binsize/2
    gauss = amp1*np.exp(-(x-mu1)**2 / (2*s**2)) + amp2*np.exp(-(x-mu1/2)
    **2 / (2*s**2))

    return gauss

#---------- UltraNest Parameters for Lorentzian fit ----------

parameters1 = ['d_rot','lam', 'bet', 'n']

def prior_transform1(cube):

    params1 = cube.copy()

    for i in range(len(params1)):
        params1[i] = cube[i] * (hi[i]-lo[i]) + lo[i]

    return params1

def lor_likelihood(params1):

    d_rot, lam, bet, n = params1
    y_model = lorentzian(x, d_rot, lam, bet, n)
```

```
    like = -0.5 * (((y_model - y) / yerr1)**2).sum()

    return like

def lorentzian(x, d_rot, lam, bet, n):

    lorentzian = d_rot * (1 - lam / (1+((1/bet)*(x-n))**2))

    return lorentzian

#---------- UltraNest Parameters END ----------
#---------- General definitions ----------

def preselecting_data(filename):
    """ Reads and reduces mode files, and returns dipole_modes, pure_modes, header, mid, d_m_err

    Parameters
    ----------
    filename : str
        name of the mode file of a star

    Returns
    -------
    dipole_modes : array-like
        dipole modes of the star
    pure_modes : array-like
        radial modes of the star
    header : array-like
        complete header of the file
    mid : array-like
        average between two consecutive radial modes
    d_m_err: array-like
        error of dipole modes
    """

    data = pd.read_csv(filename, delimiter = ' ', skiprows = 8, skipinitialspace = True, header = None, names = ['degr', 'freq', 'freq_e', 'amp', 'amp_e', 'tau', 'tau_e', 'ev', 'ev1'])

    dipole_ev1 = data[(data['degr'] == 1)]
    dipole_modes = dipole_ev1.iloc[:,[0,1,-1]]
    d_m_err= dipole_ev1.iloc[:,[2]]

    pure_ev = data[(data['degr'] == 0)]
    pure_modes = pure_ev.iloc[:,[0,1,-2]]

    mid = np.array([])
    for i in range(len(pure_modes)-1):
        mid = np.append(mid, ((pure_modes.iloc[i,1] + pure_modes.iloc[i+1,1])/2))

```

```
    data_head = pd.read_csv(filename, delimiter = ' ', skiprows = 5,
    nrows = 1, skipinitialspace = True, header = None, names = ['fmax', '
    fmax_e', 'dnu', 'dnu_e', 'dnu_cor', 'du_cor_e', 'dnu02', 'dnu02_e', '
    f0_c', 'f_0_c_e', 'alpha', 'alpha_e', 'evo'])

    header = data_head.iloc[:,[0, 2, 6, 8, 10, -1]]

    return dipole_modes, pure_modes, header, mid, d_m_err


def find_nearest(data_array, value):
    """ function that finds the closest value in a sample

    Parameters
    ----------
    data_array : array-like
        radial modes (pure_modes)
    value: float
        tested value for closest approach

    Returns:
        data_array[idx] : array-like
            array with closest values
    """

    data_array = np.asarray(data_array)
    idx = (np.abs(data_array - value)).argmin()

    return data_array[idx]

def rot_split(d_split, dnu, nu, nu_p1):
    """ function that creates guessed values for d_rot

    Parameters
    ----------
    d_split : float
    dnu : float
        large frequency separation
    nu : float
        dipole mode frequency
    nu_p1 : float
        frequency of the theoretical pure pressure mode

    Returns
    -------
    d_rot : array-like
        guessed values for d_rot
    """

    lam = (0.33 + 0.013*dnu) * (1+ 0.12*np.random.normal(0,1))
    bet = (0.03 + 0.003*dnu) * (1 + 0.22*np.random.normal(0,1))

```

```python
    d_rot = d_split* ((1 - lam / (1 + ((nu - nu_p1)/(bet*dnu))**2))**(-1))

    return d_rot

def histogram(data_array):

    y, bins, patches = plt.hist(data_array, bins = round(len(data_array)**(1/2)), density = True, histtype = 'step')
    plt.xlabel(r"${\delta\nu}_{rot}$ $[\mu Hz]$")
    plt.ylabel("Histogram")

    return y, bins, patches

def split_mode(nu, dnu, nu_p1, d_rot):
    """ calculates the potential rotational splitting

    Parameters
    ----------
    nu : float
        dipole mode frequency
    dnu : float
        large frequency separation
    nu_p1 : float
        frequency of the theoretical pure pressure mode
    d_rot : float
        guessed value for d_rot

    Returns
    -------
    nu_split : array-like
        estimate of the rotational splitting
    """

    lam = (0.33 + 0.013*dnu)
    bet = (0.03 + 0.003*dnu)

    nu_split = nu + d_rot * ((1 - lam / (1 + ((nu - nu_p1)/(bet*dnu))**2)))

    return nu_split


#---------- Begin program ----------

if __name__ == "__main__":

    t_start = perf_counter()

    stars = np.genfromtxt(config['file_paths']['input_file_split'], dtype=str, encoding = None)

    if stars.size == 1:
```

```
        stars = (stars,)
    n_stars = len(stars)
    print(f"Star analysis of {n_stars} stars.")

    for i, star in enumerate(stars):
        file_names = glob.glob(f"{config['file_paths']['path_data']}{star}.modes.dat")
        print(star)

        for k, filename in enumerate(file_names):
            data_array, pure_modes, header, f_mid, d_m_err = preselecting_data(filename)

            img = WImage(filename = f"{config['file_paths']['path']}{star}.echelle.pdf", resolution = 300) # presents the echelle diagram of each star to make a first guess, if there is a singlet, duplet, or triplet structure visible
            display(img)

            p = 0
            while p == 0:
                Rotation = np.array([])

                for m in range(len(data_array)):
                    for n in range(5):
                        if m+n < len(data_array):
                            d_split_guess = data_array.iloc[m+n,1] - data_array.iloc[m,1]
                            if d_split_guess < header.iloc[0,1]/6:
                                for k in range(100):
                                    pure = find_nearest(f_mid, data_array.iloc[m,1])
                                    rot = rot_split(d_split_guess, header.iloc[0,1], data_array.iloc[m,1],pure)
                                    if rot > 0 :
                                        Rotation = np.append(Rotation, rot)

                fig = plt.figure()
                n, bins, patches = histogram(Rotation)
                y = n
                yerr = np.ones(len(y))*np.mean(d_m_err.iloc[:,0])
                x = bins[:-1]
                y_max_value = y.max()
                x_value = x[y.argmax()]

                print(f"Guessed Rotational Splitting: {x_value}")

# ---------- Gaussian Fit ----------
                binsize = np.mean(np.diff(bins))
                lo = (0,0, x_value*0.5)
                hi = (y_max_value*2,y_max_value*2, x_value*1.2)
```

```
                sampler = ultranest.ReactiveNestedSampler(parameters, my_likelihood, prior_transform)
                result = sampler.run(min_num_live_points=400, dKL=np.inf, min_ess=100)
                sampler.print_results()
                par = np.array(result['posterior']['median'])
                fit = gaussian(x, *par )

                plt.plot(x,fit)
                plt.title(f"KIC{star}, " + r"$\Delta\nu = $" + f"{header.iloc[0,1]}, " + r"$\nu_{\mathrm{max}} = $"f"{header.iloc[0,0]}")
                plt.xlim(0,x.max()*1.5)
                gauss = par[1]/2
                stdev = result['posterior']['stdev']
                mean = result['posterior']['mean']
                plt.text(4.5,y_max_value*0.9, r"$\delta\nu_{\mathrm{rot, guessed}} = $" + f"{round(gauss,3)}")
                plt.show()

                a = int(input('Good Gaussian? [y1/n0] ' ))

                if a == 1:

                    b = input('[2/1] ?')
                    dd = int(b)
                    rot_max = gauss/dd

                    nu = np.array([])
                    split = np.array([])

                    for j in range(len(data_array)):
                        pure = find_nearest(f_mid, data_array.iloc[j,1])
                        split_m = split_mode(data_array.iloc[j,1], header.iloc[0,1], pure, rot_max)
                        nu_split = abs(data_array.iloc[j,1]-split_m)
                        split = np.append(split, nu_split)
                        nu = np.append(nu, data_array.iloc[j,1])

                    df = pd.DataFrame({'nu': nu, 'split': split})

#---------- Identifying Triplets ----------

                    modes = np.array([])
                    true_split = np.array([])
                    used = np.array([])

                    v = 0.10
                    k = 0

                    while k+2 <= len(df):
                        v_guess_m = df.iloc[k,0] + df.iloc[k,1] - df.iloc[k,1]*v
```

```
    v_guess_p = df.iloc[k,0] + df.iloc[k,1] + df.iloc[k,1]*v

    mod_spl = np.array([])

    for l in range(len(df)):
        if v_guess_m <= df.iloc[l,0] <= v_guess_p:
            mod_spl = np.append(mod_spl, df.iloc[l,0])

    if len(mod_spl) != 0:
        nearest = find_nearest(mod_spl, df.iloc[k,0] + df.iloc[k,1])

        v_nearest_m = nearest + df.iloc[k,1] - df.iloc[k,1]*v
        v_nearest_p = nearest + df.iloc[k,1] + df.iloc[k,1]*v

        mod_spl_1 = np.array([])

        for l in range(len(df)):
            if v_nearest_m <= df.iloc[l,0] <= v_nearest_p:
                mod_spl_1 = np.append(mod_spl_1, df.iloc[l,0])

        if len(mod_spl_1) != 0:
            nearest_fin = find_nearest(mod_spl_1, nearest+df.iloc[k,1])

            tru_spl = abs((df.iloc[k,0] - nearest)+(nearest-nearest_fin))/2
            modes = np.append(modes, nearest)
            true_split = np.append(true_split, tru_spl)
            used = np.append(used, df.iloc[k,0])
            used = np.append(used, nearest)
            used = np.append(used, nearest_fin)

            k += 1
        else:
            k += 1

    else:
        k += 1

lis = []
for b in range(len(used)):
    for c in range(len(df)):
        if used[b] == df.iloc[c,0]:
            lis.append(c)

```

```
                    modi = df.drop(lis)
                    modified = modi.reset_index(drop = True)

#---------- Identifying Duplets ----------

                    k = 0
                    while k+1 <= len(modified):
                        v_guess_m = modified.iloc[k,0] + 2 * modified.iloc[k,1] - modified.iloc[k,1]*v
                        v_guess_p = modified.iloc[k,0] + 2 * modified.iloc[k,1] + modified.iloc[k,1]*v

                        mod_spl = np.array([])

                        for l in range(len(modified)):
                            if v_guess_m <= modified.iloc[l,0] <= v_guess_p:
                                mod_spl = np.append(mod_spl, modified.iloc[l,0])

                        if len(mod_spl) != 0:
                            nearest = find_nearest(mod_spl, modified.iloc[k,0] + 2*modified.iloc[k,1])

                            tru_spl_ = abs(modified.iloc[k,0]-nearest)/2
                            z_comp = modified.iloc[k,0] + tru_spl_
                            modes = np.append(modes, z_comp)
                            true_split = np.append(true_split, tru_spl_)
                            used = np.append(used, modified.iloc[k,0])
                            used = np.append(used, nearest)

                            k += 1
                        else:
                            k += 1

                    if len(true_split) >= 3:

                        dnu = header.iloc[0,1]

                        nu_p1 = np.array([])

                        for n in range(len(modes)):
                            pure = find_nearest(f_mid, modes[n])
                            nu_p1 = np.append(nu_p1, pure)

#---------- Lorentzian Fit ----------

                        fig, ax = plt.subplots()
                        fig.set_size_inches(20, 4.2)

                        x = (modes-nu_p1)/dnu
                        y = true_split

```

```
                    yerr1 = np.ones(len(x))*np.mean(d_m_err.iloc[:,0])/5

                    plt.plot(x,y, 'x')
                    plt.xlim(-0.5,0.5)
                    plt.xlabel(r'$(\nu-\nu_{p1})/\Delta \nu$')
                    plt.ylabel(r'$\delta \nu_{\mathrm{split}} [\mu Hz]$')

                    sm = true_split.max()
                    lo = (0.5*sm, 0, 0, -1*dnu)
                    hi = (1.5*sm, 0.1*dnu, 0.01*dnu, 1*dnu)
                    sampler = ultranest.ReactiveNestedSampler(parameters1, lor_likelihood, prior_transform)
                    result = sampler.run(min_num_live_points=400, dKL=np.inf, min_ess=100)
                    sampler.print_results()
                    par = np.array(result['posterior']['median'])
                    print(par)
                    stdev = result['posterior']['stdev']
                    mean = result['posterior']['mean']

                    u = round(par[0], 3)
                    x = np.linspace(-1,1,1000)
                    fit = lorentzian(x, *par )
                    ax.xaxis.set_minor_locator(MultipleLocator(0.02))
                    ax.yaxis.set_minor_locator(MultipleLocator(0.005))
                    plt.tick_params(right = True, which = 'minor')
                    plt.tick_params(top = True, which = 'minor')
                    plt.tick_params(right = True, which = 'major')
                    plt.tick_params(top = True, which = 'major')
                    plt.title(f"KIC{star}, " + r"$\Delta\nu = $" + f"{header.iloc[0,1]}, " + r"$\nu_{\mathrm{max}} = $"f"{header.iloc[0,0]}")
                    plt.text(0.35,0.325, r"$\delta\nu_{\mathrm{rot}} = $" + f"{u}" + r"$\mu Hz$")
                    plt.plot(x,fit, '--')
                    plt.show()
                else:
                    print('No splitting')
            p += a

    p = (i+1)/n_stars
    sys.stdout.write("\r")
    sys.stdout.write("[%-30s] %d%%" % ("="*int(30*p), 100*p))
    t_left = (perf_counter() - t_start) / (i+1) * (n_stars - i-1)
    sys.stdout.write(f"; est. t until done: {t_left:.1f} s")
    sys.stdout.flush()

t_elap = perf_counter() - t_start
print(f"\nAnalysed {n_stars} stars in {t_elap:.2f} seconds.")
```

```
    print(f"Average time per star: {t_elap/n_stars:.2f} seconds.")
```

Listing A.1: Full Python Code